

Electronic band structure of Ti_2O_3 thin films studied by angle-resolved photoemission spectroscopy

Naoto Hasegawa¹, Kohei Yoshimatsu^{1,2,*}, Daisuke Shiga¹, Tatsuhiko Kanda¹, Satoru Miyazaki¹, Miho Kitamura³, Koji Horiba³, and Hiroshi Kumigashira^{1,2,3}

¹ *Institute of Multidisciplinary Research for Advanced Materials (IMRAM), Tohoku University, Sendai, 980–8577, Japan*

² *Materials Research Center for Element Strategy (MCES), Tokyo Institute of Technology, Yokohama 226–8503, Japan*

³ *Photon Factory, Institute of Materials Structure Science, High Energy Accelerator Research Organization (KEK), Tsukuba, 305–0801, Japan*

Abstract

Ti_2O_3 exhibits a unique metal–insulator transition (MIT) at approximately 450 K over a wide temperature range of ~ 150 K. This broad MIT accompanied by lattice deformation differs from the sharp MITs observed in most other transition-metal oxides. A long-standing issue is determining the role of electron–electron correlation in the electronic structure and MIT of Ti_2O_3 . However, the lack of information about the band structure of Ti_2O_3 has hindered investigating the origin of its unusual physical properties. Here, we report the electronic band structure of “insulating” Ti_2O_3 films with slight hole doping by angle-resolved photoemission spectroscopy (ARPES). ARPES showed clear band dispersion on the surface of single-crystalline epitaxial films. The experimentally obtained band structures were compared with band-structure calculation results based on density functional theory (DFT) with generalized gradient approximation + U correction. The obtained band structures are in good agreement with the DFT calculations at $U = 2.2$ eV, suggesting that electron–electron correlation plays an important role in the electronic structure of Ti_2O_3 . Furthermore, the detailed analyses with varying U suggest that the origin of the characteristic MIT in Ti_2O_3 is a semimetal–semimetal or semimetal–semiconductor transition caused by changes in the Fermi surface due to lattice deformation.

*Correspondence: kohei.yoshimatsu.c6@tohoku.ac.jp

INTRODUCTION

Ti₂O₃, which has a corundum-type crystal structure, exhibits a unique metal–insulator transition (MIT). The bulk Ti₂O₃ is a nonmagnetic insulator with a small bandgap energy of approximately 100 meV [1] at low temperatures, and it shows a transition to semimetallic states at temperatures of approximately 450 K [2–9], which extends over a broad temperature of ~150 K. This is a unique type of transition that is not observed in most other transition-metal oxide systems. Although the crystal symmetry remains unchanged across the MIT, the unit-cell c/a ratio changes significantly, which suggests a close relationship between the MIT and lattice deformations [2–6, 9–12].

Over the past few decades, the MIT mechanism has been experimentally and theoretically investigated [1–32]. The most relevant phenomenon in this mechanism is the overlap of the a_{1g} and e_g^π bands due to the Ti–Ti distance modulations along the c -axis of the crystal lattice [5, 6]. Owing to the trigonal distortions, the t_{2g} levels in TiO₆ octahedra further split into a lower non-degenerate a_{1g} level and higher double-degenerate e_g^π levels. The a_{1g} orbitals between the face-shared TiO₆ octahedra along the c -axis are strongly hybridized to form a_{1g} and a_{1g}^* bands with e_g^π bands between them. When the Ti–Ti bond distances along the c -axis are short, the energy splitting between the a_{1g} and a_{1g}^* bands becomes large, and consequently, the e_g^π bands do not overlap with the a_{1g} bands. Furthermore, only the a_{1g} band is completely filled with Ti 3*d* electrons; therefore, Ti₂O₃ acts as an insulator.

The Ti₂O₃ energy diagram describes its electronic structures and reveals the close connection between the MIT and c/a ratio. In fact, the a -axis and c -axis lattice constants of bulk Ti₂O₃ vary significantly with temperature, and the c/a ratio increases from 2.648 to 2.701 in the range of 373 to 553 K across the MIT [3]. The modulation of Ti 3*d* electron occupations in the a_{1g} orbitals associated with a change in the c/a ratio was revealed from the temperature

dependence of linear dichroism in Ti $2p$ X-ray absorption spectra [8, 14, 15].

However, the band-structure calculations challenge the validity of this simple phenomenological model because the a_{1g} and e_g^π bands always overlap for typical Ti–Ti distances [10]; a short Ti–Ti distance of less than 2.2 Å is required to form the aforementioned insulating band diagram, which suggests the importance of electron–electron correlations in Ti_2O_3 . To better understand the unusual physical properties of Ti_2O_3 , it is necessary to collect detailed information about the complicated electronic band structure of the material.

Angle-resolved photoemission spectroscopy (ARPES) is a unique and powerful experimental technique for determining the band structure of a solid and has long played a central role in studies of the electronic properties of strongly correlated electron systems [33–49]. However, there have been few ARPES studies on Ti_2O_3 with three-dimensional corundum-type crystal structures [19]. This is mainly due to the difficulty in obtaining single-crystal surfaces of Ti_2O_3 using standard surface-preparation techniques, such as cleaving or sputtering and annealing. In addition, the chemically active surface of Ti_2O_3 [23] restricts surface-sensitive ARPES measurements on chemically well-defined surfaces. Thus, the lack of information about the band structures near the Fermi level (E_F), especially the Fermi surface (FS), has limited the understanding of the physics of Ti_2O_3 .

In this study, to elucidate the electronic structure near E_F of Ti_2O_3 , we performed soft-X-ray (SX) ARPES [42–49] on single-crystalline epitaxial Ti_2O_3 films grown on $\alpha\text{-Al}_2\text{O}_3$ substrates. We synthesized the films with slight hole doping by laser molecular beam epitaxy (MBE) to obtain an atomically flat and well-ordered surface. By using the well-defined surface of the epitaxial films, we clearly observed the electronic band structure of Ti_2O_3 . The Ti $3d$ -derived hole band forms an open triangular-pyramidal-vase-shaped FS along the Γ –A line in the hexagonal Brillouin zone (BZ). The experimental band structures were compared with the

band-structure calculations based on density functional theory (DFT) with generalized gradient approximation (GGA) + U correction. Detailed analysis with varying U revealed that the obtained band structures are well-described by the DFT calculations at $U=2.2$ eV, indicating that the electron–electron correlation plays an important role in the electronic structure of Ti_2O_3 . Furthermore, the comparison between the ARPES results and DFT + U calculations with varying U and c/a ratio suggests important implications regarding the origin of the characteristic MIT in Ti_2O_3 ; the MIT is a semimetal–semimetal or semimetal–semiconductor transition caused by changes in the FS due to lattice deformation.

EXPERIMENTAL

Epitaxial Ti_2O_3 films with a thickness of approximately 100 nm were grown on $\alpha\text{-Al}_2\text{O}_3$ (0001) substrates by laser MBE. A sintered TiO_x pellet was used as the ablation target [50]. A Nd:Y₃Al₅O₁₂ (Nd:YAG) laser was used for the target ablation using its third harmonic wave ($\lambda = 355$ nm) with a fluence of approximately 1.5 J/cm² and repetition rate of 5 Hz. Prior to film growth, $\alpha\text{-Al}_2\text{O}_3$ substrates were annealed in air at 1100°C for 2 h to obtain an atomically flat surface with step-and-terrace structures. During the deposition, the substrate temperature was maintained at 1000°C, and the oxygen pressure was maintained at 5×10^{-7} Torr. After deposition, the oxygen gas supply was immediately turned off, and the films were quenched to room temperature to prevent overoxidation [16, 17, 51, 52].

After growth, the films were transferred *in vacuo* to the photoemission chamber using a mobile vacuum-transfer vessel to reduce surface contamination and additional oxidation. During transportation, the samples were under an ultrahigh vacuum below 5.0×10^{-10} Torr. Photoemission spectroscopy (PES) and ARPES were conducted at the BL-2A MUSASHI

beamline of the Photon Factory, KEK. The PES spectra were recorded at 100 K using a VG-Scienta SES-2002 analyzer with total energy resolutions of 250 and 500 meV at photon energies ($h\nu$) of 800 and 1486 eV, respectively. In the ARPES experiments in the SX region of $h\nu = 300$ –640 eV, the energy and angular resolutions were set to approximately 150–250 meV and 0.25° , respectively. The ARPES experiments were also conducted at 100 K in the p -polarization geometry [36–40]. E_F was inferred from gold foil in electrical connection with the sample. The surface structure and cleanliness of the vacuum-transferred films were examined by low-energy electron diffraction (LEED) and core-level photoemission measurements immediately before the ARPES measurements. The LEED pattern of the films showed six sharp diffraction spots on a low background, as shown in Fig. 1(a), reflecting the long-range crystallinity and cleanliness of the surface. No detectable C 1s peak was observed in the core-level photoemission spectra (not shown). These results indicate that the Ti_2O_3 films have high surface crystallinity and cleanliness required for ARPES measurements.

The surface morphology of the measured Ti_2O_3 films was analyzed by *ex-situ* atomic force microscopy (AFM) in air, and atomically flat surfaces were observed, as shown in Fig. 1(b). The crystal structure was characterized by X-ray diffraction (XRD) (see Fig. S1 in the Supplemental Material [50]), which confirmed the epitaxial growth of single-phase Ti_2O_3 films on the substrates. The out-of-plane and in-plane epitaxial relationships were Ti_2O_3 [0001] // α - Al_2O_3 [0001] and Ti_2O_3 [11–20] // α - Al_2O_3 [11–20], respectively. The temperature dependence of the electrical resistivity was measured using the standard four-probe method. The transport properties were in good agreement with previously reported values [16] (see Fig. S2 in the Supplemental Material [50]). Detailed characterizations of the grown films are presented in the Supplemental Material [50].

DFT-based band-structure calculations were conducted using QUANTUM ESPRESSO

software [53, 54]. The Perdew–Burke–Ernzerhof generalized gradient approximation (PBE-GGA) was adopted as the exchange-correlation functional [55]. The kinetic energy (charge density) cut-off was set to 60 (600) Ry. The Ti and O atomic positions were optimized by the Monkhorst–Pack scheme using a $6 \times 6 \times 6$ k -point grid in a self-consistent scheme [56]. In the self-consistent calculation, the lattice parameters were fixed as the experimental values for the present film ($a = 5.102 \text{ \AA}$, $c = 13.80 \text{ \AA}$, $c/a = 2.70$), which were determined by reciprocal space mapping taken at room temperature, as shown in Fig. S1(b) in the Supplemental Material [50]. Further computing details are described in the Supplemental Material [50].

RESULTS AND DISCUSSION

Before discussing the ARPES results, we provide evidence for the fact that the properties of Ti_2O_3 are retained in the surface region of the films accessible for SX-ARPES [42–49] because the surface of Ti_2O_3 is known to be extremely sensitive to oxygen and to lose the characteristic $\text{Ti}^{3+}\text{--Ti}^{3+}$ dimer structures due to oxidation [23]. Figure 1(c) shows the Ti $2p$ core-level spectrum of the Ti_2O_3 films obtained at 100 K (insulating phase). Note that the existence of Ti^{4+} states at 459 eV due to surface overoxidation [23] is hardly seen in the spectrum. The Ti $2p$ core level exhibits the complicated multiplet structure characteristic of Ti_2O_3 single crystals [8, 23]. The close similarities in the core-level spectra between the film surface and cleaved surface of Ti_2O_3 single crystals [8, 23] support the fact that the chemical states in the films are almost the same as those in bulk. From the cluster-model calculation, the satellite structures were attributed to the strong bonding of the a_{1g} orbitals at the Ti–Ti dimer in Ti_2O_9 clusters [8]. Therefore, the existence of the multiplet structures demonstrates the formation of $\text{Ti}^{3+}\text{--Ti}^{3+}$ dimers even in the surface region of the Ti_2O_3 films.

The Ti^{3+} ($3d^1$) states in the Ti_2O_3 films are also confirmed by the valence-band spectrum (Fig. 1(d)). The spectrum mainly consists of two features: a structure derived from O $2p$ states at binding energies of 4–10 eV and a two-peak structure derived from the Ti $3d$ states near E_F [8, 20–23]. The Ti $3d$ states consist of a sharp coherent peak in the vicinity of E_F and a weak broad satellite structure centered around 2.3 eV, demonstrating the Ti^{3+} ($3d^1$) feature of Ti_2O_3 . The valence bands initially seem to be almost the same between the films and bulk, which is consistent with the results of the Ti $2p$ core-level spectra, indicating that the properties of Ti_2O_3 are retained in the surface region of the films. However, a closer inspection of E_F (inset of Fig. 1(d)) reveals that there is a small but distinct density of states at E_F in the films. Furthermore, the coherent peak of the films is shifted toward the lower-binding-energy side from that of the bulk, reflecting the higher conductivity in the films (see Fig. S2 in the Supplemental Material [50]). Based on the shift of the peak positions, the chemical-potential shift due to excess hole carriers is evaluated to be approximately 200 meV in the Ti_2O_3 films. We will discuss the value of the chemical-potential shift in connection with the ARPES results.

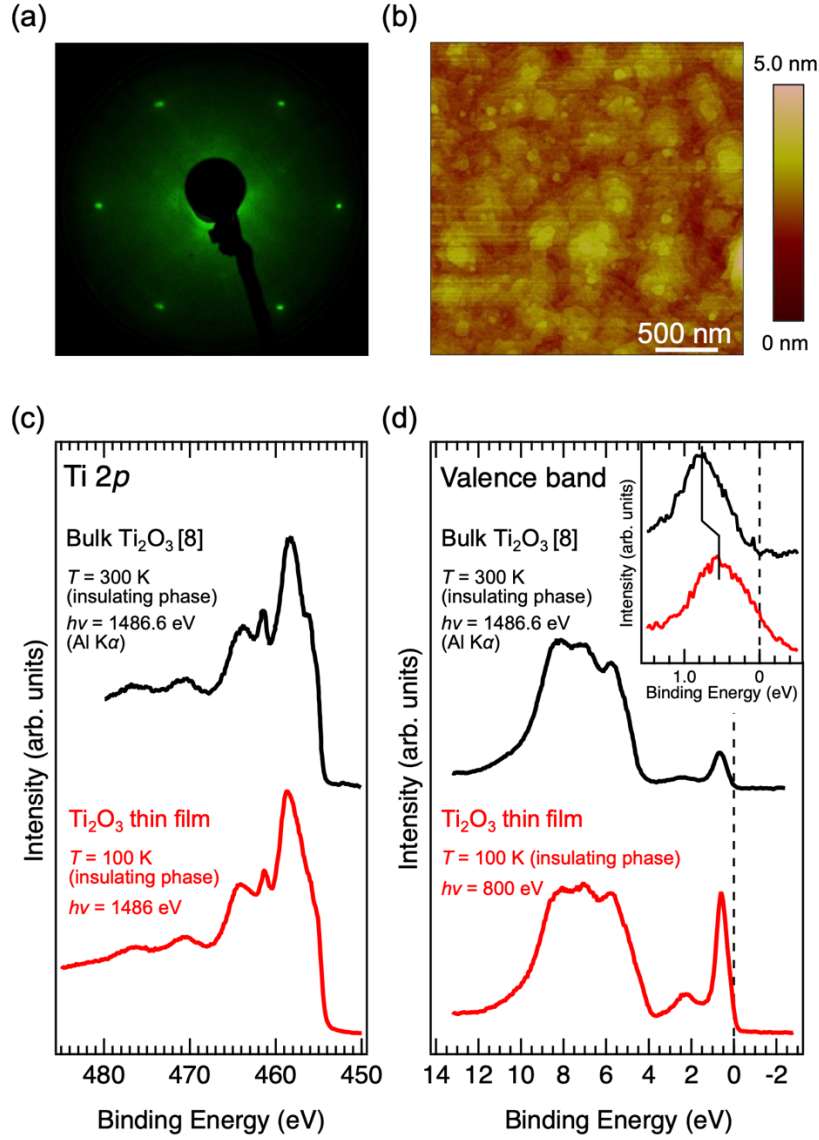


FIG. 1. (a) LEED pattern and (b) AFM image of the Ti_2O_3 films grown on $\alpha\text{-Al}_2\text{O}_3$ (0001) substrates. The hexagonal spots of the LEED pattern correspond to the surface BZ projected along the [111] direction of rhombohedral Ti_2O_3 . The root-mean-square of surface roughness of the films was estimated to be less than 1.0 nm in the AFM image with a $10 \times 10 \mu\text{m}^2$ area, demonstrating the flat surface necessary for the present spectroscopic studies. (c) Ti $2p$ core-level PES spectrum of the Ti_2O_3 films taken at 100 K (insulating phase) with a photon energy of $h\nu = 1486$ eV. (d) Corresponding valence-band spectrum taken at 800 eV. For comparison, the PES spectra of the cleaved surface of a Ti_2O_3 single crystal (black line) in an insulating phase are also shown for (c) and (d) [8]. The inset of (d) shows the comparison of the Ti $3d$ -derived coherent peaks near E_F . A clear peak shift of approximately 200 meV is observed, reflecting the hole-doped nature of the films, whereas the shape itself remains unchanged.

From the above characterizations, we have confirmed that the Ti_2O_3 films have a long-range ordered crystalline surface without the detectable overoxidation (Ti^{4+} states) required for ARPES measurements and that characteristic $\text{Ti}^{3+}-\text{Ti}^{3+}$ dimers are formed in the surface region of the film accessible for SX-ARPES. Thus, we address the band structure of the Ti_2O_3 films by ARPES. Figure 2(a) shows the schematic crystal structure of Ti_2O_3 in both the primitive rhombohedral unit cell and associated conventional hexagonal cell. The corresponding rhombohedral BZ is depicted in Fig. 2(b), together with an equivalent hexagonally shaped one [10]. For notational simplicity, we refer to the high-symmetry points and lines in the hexagonal BZ hereafter.

Figure 2(c) shows the out-of-plane FS map for the Ti_2O_3 films obtained from normal-emission ARPES measurements for the Γ -A-H-K emission plane (the blue hatched area in the BZ shown in Fig. 2(b)). Reflecting the hole-doped nature, a meandering FS that follows the periodicity of the bulk BZ is clearly observed along the BZ center line (see also Fig. S12 in the Supplemental Material [50]). The cross-section of the FS is largest at the A point, monotonically decreases away from the A point, and is smallest at the Γ point. The observed FS topology was well reproduced by the DFT + U calculation with reasonable parameters (Figs. S8 and S9 in the Supplemental Material [50]), which is discussed later. The in-plane FSs at the A-H-L emission plane (taken at 500 eV) and Γ -K-M emission plane (taken at 565 eV) are shown in Figs. 2(d). A triangular-like FS is clearly observed at the A point. The overall threefold intensity pattern of the observed FS is responsible for the trigonal symmetry of Ti_2O_3 , suggesting the bulk origin of the FS. Indeed, the triangular-like shape of the FS was reversed at the other A point of one point below [41] (see Fig. S14 in the Supplemental Material [50]). At the Γ point, the FS with a round shape is also observed. These results indicate the existence of an open FS in the Ti_2O_3 films. It should be noted that we did not observe any indication of other FSs outside the open

FS in these measurement planes. Meanwhile, the existence of another small closed hole FS around the A point is predicted from band-structure calculations [10, 50]. However, it is difficult to examine the existence of another FS inside the open FS owing to the overlap of open FS having predominant intensity (see Fig. S9 in the Supplemental Material [50]), although the existence of the other FS is suggested by normal-emission ARPES along the Γ -A direction (see Fig. S12 in the Supplemental Material [50]). Assuming a triangular-pyramidal shape of the open FS, the carrier density of the Ti_2O_3 films would be approximately $2.4 \times 10^{20} \text{ cm}^{-3}$, which is consistent with the carrier density estimated from Hall effect measurements ($1.1 \times 10^{20} \text{ cm}^{-3}$) [16].

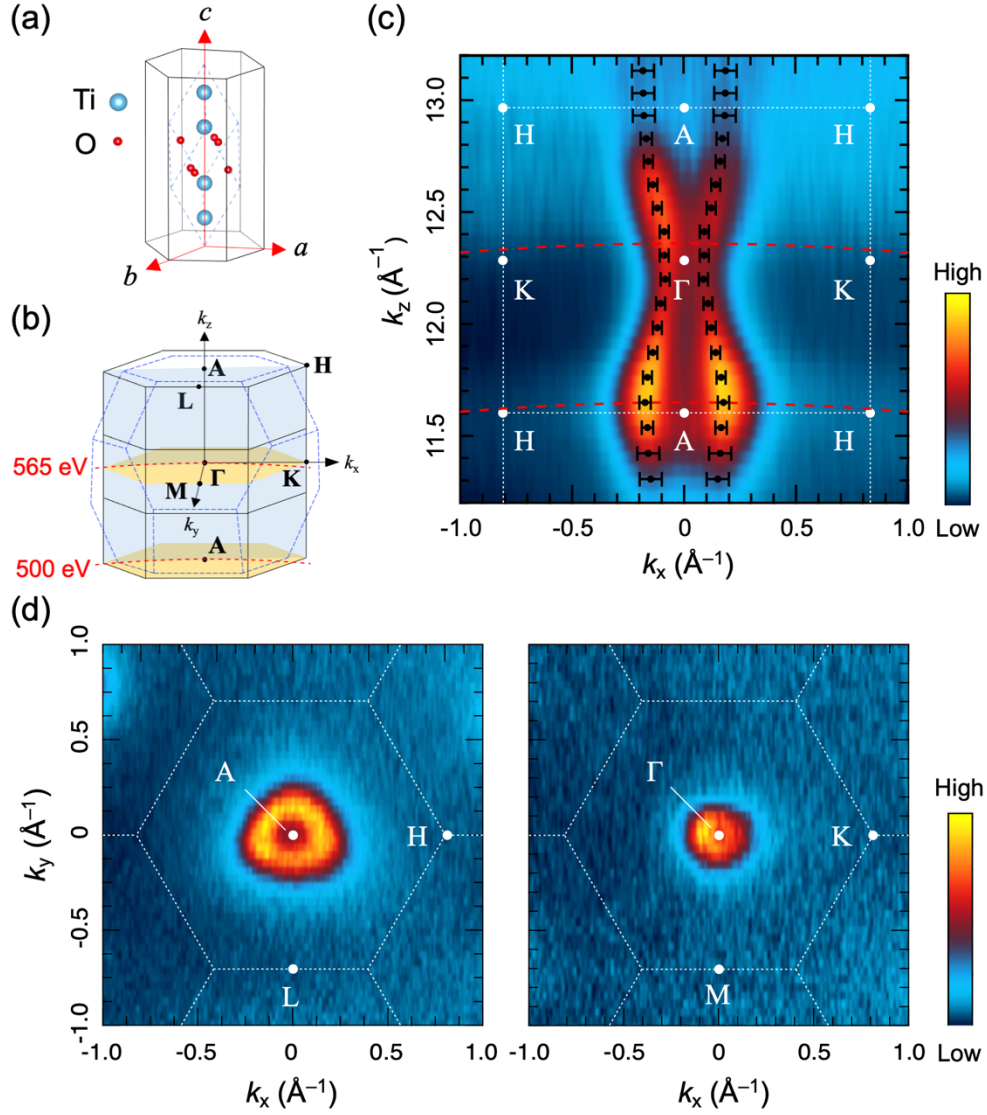


FIG. 2. (a) Crystal structure of Ti_2O_3 in primitive rhombohedral unit cell (blue dashed lines), surrounded by the conventional non-primitive hexagonal unit cell (black solid lines). The primitive rhombohedral unit cell contains two formula units, while the conventional hexagonal unit cell contains eighteen formula units. The red hexagonal unit vectors were determined to be $a = 5.102 \text{ \AA}$ and $c = 13.80 \text{ \AA}$ by XRD measurements (see Fig. S1 in the Supplemental Material [50]). (b) Corresponding rhombohedral BZ and an equivalent hexagonally-shaped one. In the hexagonal BZ, the high-symmetry points are labeled. The red dotted arc lines represent the k paths passing through the A point (at a photon energy of 500 eV) and the Γ point (at a photon energy of 565 eV). A light-blue plate represents the Γ -A-H-K emission plane where the out-of-plane FS map was measured, while two light-yellow plates represent the A-H-L and Γ -K-M emission planes for the in-plane FS mappings at corresponding energies. (c) Out-of-plane FS

map in the Γ -A-H-K emission plane obtained by varying the excitation photon energies from 470 to 640 eV. The Fermi-momentum (k_F) points determined by the ARPES spectra are indicated by data markers. (d) In-plane FS maps acquired at the constant photon energies of 500 eV (left panel: the A-H-L emission plane) and 565 eV (right panel: the Γ -K-M emission plane) by changing emission angles. The corresponding hexagonal BZ boundaries are overlaid as white lines. The FS maps were obtained by plotting the ARPES intensity within the energy window of $E_F \pm 50$ meV.

According to the band-structure calculation [10, 50], the electronic band structure near E_F of Ti_2O_3 mainly consists of the e_g^π - and a_{1g} -derived bands. The former forms flat (dispersive) bands, while the latter forms dispersive (flat) bands along the out-of-plane (in-plane) direction, reflecting their anisotropic orbital shape. The e_g^π -derived band forms an electron pocket(s) at the Γ point, whereas the a_{1g} -derived band forms a hole pocket(s) at the A point. The slight overlap between the two pockets makes intrinsic Ti_2O_3 a compensated semimetal. This semimetallic nature may be the origin of the unusual physical properties of Ti_2O_3 because the delicate balance between the energy of the e_g^π and a_{1g} states causes a notable change in the conduction-carrier character as a result of hybridization with the other states. Thus, it is worth investigating the band structure near E_F . Figure 3 shows the experimental band structures along the in-plane high-symmetry directions (the Γ -K and A-H lines in Fig. 3(a) and 3(b), respectively). The corresponding energy distribution curves (EDCs) along each line are shown in Fig. S15 [50]. As expected from the FS maps in Fig. 2, highly dispersive hole bands exist both at the Γ and A points and form an FS at the zone center, reflecting the existence of hole carriers. The bands cross E_F at Fermi momentum $k_F = 0.096 \text{ \AA}^{-1}$ (0.155 \AA^{-1}) around the Γ (A) point, while they disperse down to approximately 700 meV around the zone boundary.

To investigate the band structure near E_F in more detail, we compared the experimental band structure with the DFT calculation based on the GGA + U approximation using the reasonable parameters consistent with the experimental facts [17,50]. According to the DFT + U calculation, the band structures, especially the FS topology, of Ti_2O_3 strongly depend on the parameters of U and c/a ratio (Figs. S5–S7 in the Supplemental Material [50]). Herein, we used $U = 2.2$ eV to reproduce the insulating phase of bulk Ti_2O_3 , which exhibits an energy gap of approximately 100 meV at a c/a ratio of 2.639 [17]. Moreover, the c/a ratio, which also governs the electronic properties of Ti_2O_3 , was fixed at 2.70 as determined from the XRD measurements (see Fig. S1 in the Supplemental Material [50]). The results of the DFT calculations are shown in the panels of Fig. 3, where the Fermi level in the DFT calculations is shifted by 180 meV toward the higher-binding-energy side to reproduce the k_F value of the hole pocket at the Γ point. This is because the electron pocket is always formed at the Γ point in DFT calculations irrespective of U values and c/a ratios for Ti_2O_3 with metallic ground states (see Figs. S5–S7 in the Supplemental Material [50]). It should be noted that the shift of the Fermi level is consistent with the chemical-potential shift estimated from the shift of the Ti $3d$ coherent peak, as seen in the inset of Fig. 1(d).

The ARPES results and DFT calculations show fairly good agreement. According to the orbital projected band structures shown in Fig. 3 (also see Fig. S4 in the Supplemental Material [50]), the hole band centered at the Γ point is assigned to the e_g^π -derived band. The hole band has a substantial e_g^π character at the Γ point, while it loses the e_g^π character rapidly apart from the zone center owing to strong hybridization with other states. Meanwhile, the other hole FSs centered at the A point fundamentally consist of two a_{1g} -derived hole bands, which degenerate along the A–H line. The a_{1g} -derived hole bands have an a_{1g} character at the A point, while they are strongly hybridized with the e_g^π and e_g^σ states apart from the zone center. As can be seen in

Fig. 3, the present ARPES results predominately show the band to have significant e_g^π -orbital weight owing to the dipole selection rules for p polarization of the incident light and measurement geometry used [33, 34, 57].

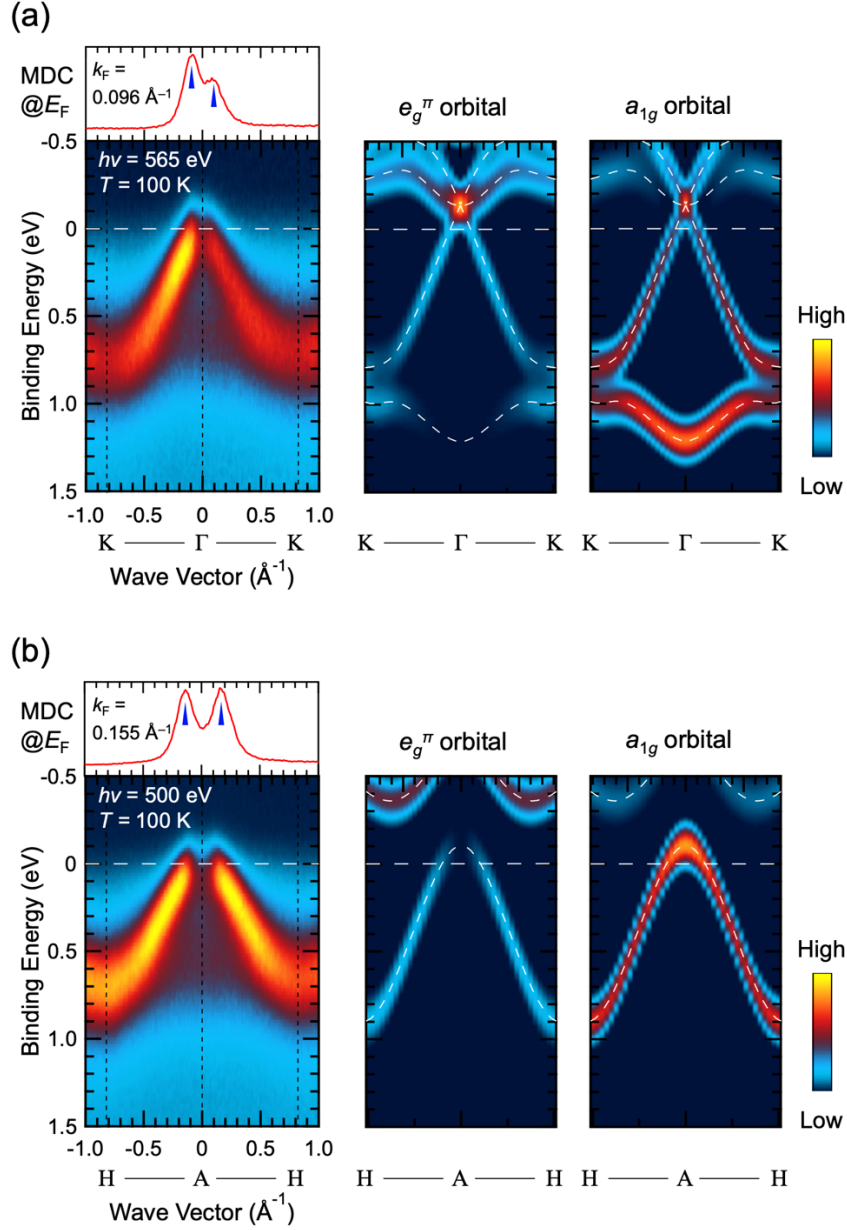


FIG. 3. Experimental band structure of the Ti_2O_3 films obtained by ARPES measurements (left panels) along the (a) Γ -K and (b) A-H high-symmetry lines, together with e_g^π (middle panels) and a_{1g} (right panels) orbital projected band structures. The corresponding k paths are illustrated in Fig. 2(c). Note that the experimental band structure is slightly asymmetric at the zone boundary, reflecting the rhombohedral BZ. The momentum distribution curves (MDCs) at E_F with an energy window of ± 5 meV are shown in the upper panel for each experimental band structure. The blue triangles indicate the Fermi momentum (k_F). In the orbital projections, the band structure is overlaid by white dotted lines.

Next, to demonstrate the importance of electron-electron correlation, we compare the band dispersion determined by ARPES with the DFT calculation in more detail. Figure 4 shows the band dispersion drawn based on the ARPES peak positions determined from the EDCs and MDCs, together with the DFT + U calculations. The band-structure calculation was also conducted at $U = 0$ eV as a reference for clarifying the effect of the electron-electron correlation. Note that the band dispersion of $U = 0$ eV is almost identical to that previously reported [10]. As can be seen in Fig. 4, the overall band structure is in good agreement with the DFT calculation at $U = 2.2$ eV; the dispersion of the e_g^π -derived hole band centered at the Γ point is quite well-reproduced. In addition, k_F along the A–H direction shows excellent agreement between the experiment and calculation, indicating the validity of $U = 2.2$ eV and the Fermi level correction for describing the electronic structures of the hole-doped Ti_2O_3 films.

Meanwhile, in the calculation, a flat band exists at a higher binding energy along the Γ –K direction. The flat band originates from the a_{1g} orbital and forms a hole pocket at the A point, reflecting the anisotropic feature of the a_{1g} orbital with a large distribution along the [0001] direction (Fig. S4 in the Supplemental Material [50]). The band is barely seen in the ARPES images in Fig. 3(a), although the existence of the a_{1g} -derived band itself is confirmed by normal emission ARPES along the Γ –A direction (see Figs. S12 and S13 in the Supplemental Material [50]). The very weak intensity is probably caused by the dipole selection rules for the a_{1g} orbital in the present experimental geometry [36–40], as demonstrated in Fig. 3(a). Furthermore, the presence of a broad nondispersive component at 0.5–0.6 eV masks the details of the band dispersion along the Γ –K direction. Therefore, it is difficult to determine the energy position of the band at the Γ point from the present data. The nondispersive states can also be seen in the ARPES image along the A–H direction (Fig. 3(b)), where such a flat band is not predicted by the DFT calculation (Fig. 4(b)). It should be noted that in contrast to the case of CrO_2 [43], such

nondispersive states cannot be found in the DFT calculation even with increasing U (see Fig. S5 in the Supplemental Material [50]) for the case of Ti_2O_3 . Although the origin of the nondispersive states is currently not clear, similar nondispersive quasi-localized states other than the lower Hubbard band (incoherent part) have also been observed in V_2O_3 [42], implying that these nondispersive states are a common feature at the surface of corundum-type conductive oxides.

In contrast to $U = 2.2$ eV, there is less agreement between the experiment and calculation at $U = 0$ eV. In particular, a significant discrepancy is observed in the a_{1g} -derived bands along the A–H direction (Fig. 4(b)). Note that we attempted to adjust the Fermi level for $U = 0$ eV to improve this discrepancy, but we did not find any improvement in the k_F positions along with both the Γ –K and A–H directions. These results suggest the importance of the electron–electron correlation for describing the electronic structure of Ti_2O_3 .

The disagreement between the experiment and calculation at $U = 0$ eV likely originates from the difference in the energy levels of the a_{1g} and e_g^π states. For the band dispersions in the DFT + U calculations with varying U (see Figs. S5 and S6 in the Supplemental Material [50]), the energy separation between the a_{1g} and e_g^π states increases with increasing U ; the a_{1g} -derived band is pushed down, whereas the e_g^π -derived band is pushed up. The increment of U causes narrowing of the a_{1g} -derived band dispersion along the A–H direction and widening of the e_g^π -derived band dispersion along the Γ –K direction. As a result, the electron and hole pockets at the Γ and A points, respectively, simultaneously become smaller, and eventually a tiny energy gap opens at $U = 2.5$ eV. Accordingly, the occupancy of the lowest-lying a_{1g} state increases with increasing U .

The semimetallic ground states of Ti_2O_3 predominantly originate from the slight overlap between the e_g^π -derived electron pocket at the Γ point and the a_{1g} -derived hole pockets at the A

point (at the midpoint of the Γ -A line for $U = 2.2$ eV) (see Fig. S5 in the Supplemental Material [50]). The increment of U reduces the degree of the overlap. Therefore, the excellent agreements in k_{FS} between the ARPES and DFT calculations at $U = 2.2$ eV indicate that the electron-electron correlation plays an essential role in the band structures of Ti_2O_3 . The sensitivity of k_{F} (FS topology) to U triggers an additional check for the validity of $U = 2.2$ eV to describe the electronic band structure of the Ti_2O_3 films. Difference in k_{F} at the A point between the ARPES and DFT calculations with varying U (Figs. S10 and S11 in the Supplemental Material [50]) suggests that the best match is obtained at $U = 2.2$ eV. This indicates the validity of the U value of 2.2 eV.

The importance of electron-electron correlation is further supported by the ARPES results shown in Fig. 4, where an almost identical bandwidth between the experiment and calculation is observed along both the Γ -K and A-H lines. Meanwhile, reduction of the overlapping was also achieved by shortening the Ti-Ti bond distances along the c -axis (or equivalently, by reducing the c/a ratio) (see Fig. S7 in the Supplemental Material [50]), although an unusually short Ti-Ti distance of less than 2.2 Å was required to form the insulating ground state in Ti_2O_3 without U [10]. Thus, it should be considered that the FS topology of Ti_2O_3 is governed by a delicate balance between the electron-electron correlations and lattice deformations and, consequently, is very sensitive to both. Besides, it should be bear in mind that the present study has not ruled out the possible contribution of dynamic electronic correlations to the MIT, namely the possibility of Ti-Ti dimer deformation assisted Mott transition in Ti_2O_3 [25]. Thus, a more elaborate band-structure calculation that adjusts both the effects and incorporates the dynamic electronic correlations in a realistic manner is necessary to reproduce the ARPES results as well as the physical properties of Ti_2O_3 [11, 24, 25].

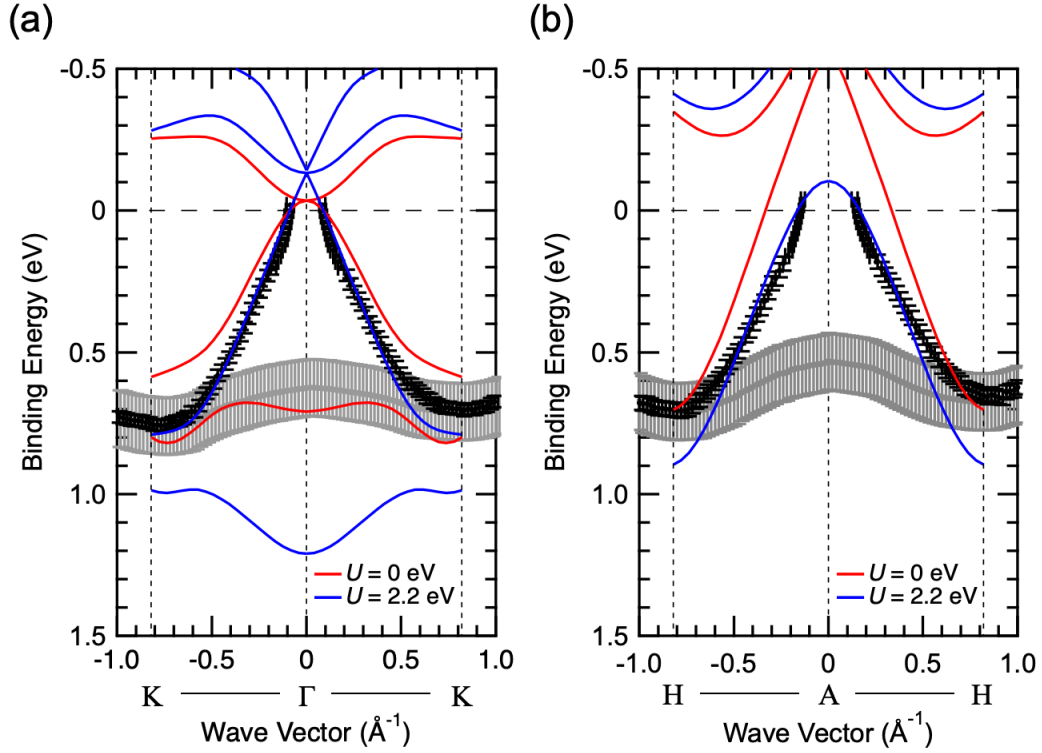


FIG. 4. Comparison of the experimental band structure and GGA+ U calculation. Peak positions determined from EDCs and MDCs are plotted by the data markers. The black and gray markers indicate the peak positions of the dispersive and nondispersive quasi-localized states, respectively. The results of GGA+ U calculation with $U = 0$ and 2.2 eV are plotted as the red and blue lines, respectively. The Fermi level of the band structure calculations with $U = 2.2$ eV (0 eV) was shifted by 180 meV (150 meV) toward the higher-binding-energy side to reproduce the experimental k_F value at the Γ point. The sudden upturn of band dispersion starting from E_F may originate from the interplay of the energy resolution and Fermi-edge cutoff [58].

Finally, we discuss the possible origin of the MIT in Ti_2O_3 . From the band structure shown in Fig. 4 (also see Fig. S3 in the Supplemental Material [50]), “intrinsic” Ti_2O_3 exhibits a semimetallic band structure, where the electron pocket at the Γ point and hole pocket at the midpoint of the Γ –A line for $U = 2.2$ eV (at the A point for $U = 0$ eV) slightly overlap in energy. In general, for such a small carrier system, the influence of the electron–electron correlation on phase-transition phenomena is not significantly large [32], whereas a slight change in a band structure significantly changes the FS topology and resultant transport properties. Meanwhile, it is known that lattice deformation occurs in Ti_2O_3 regardless of the doping concentration [3, 7, 31]. Therefore, the most plausible scenario is that the MIT of Ti_2O_3 is a semimetal–semimetal or semimetal–semiconductor transition caused by the changes in the FS topology due to lattice deformation, not a filling-controlled MIT [32]. In fact, the “MIT temperature” of $(\text{Ti}_{1-x}\text{V}_x)_2\text{O}_3$ remains almost unchanged with x , even though the carrier density changes notably; consequently, the ground state changes from insulator at $x = 0$ to metal at $x = 0.06$ [7]. To verify the possibility of semimetal–semimetal or semimetal–semiconductor transition in Ti_2O_3 caused by the changes in the FS topology due to lattice deformation, further investigations are required; in particular, detailed temperature-dependent studies on both the crystal and electronic structures are necessary.

CONCLUSION

To investigate the electronic band structure near E_F of Ti_2O_3 , we performed SX-ARPES on single-crystalline epitaxial Ti_2O_3 films grown on $\alpha\text{-Al}_2\text{O}_3$ substrates. Using well-defined surfaces of the epitaxial films, we clearly observed the electronic band structure of Ti_2O_3 . The Ti $3d$ -derived band forms an open hole FS with a triangular-pyramidal vase shape along the Γ -A line in the hexagonal BZ, which is in line with the previous transport measurements. We also found the highly dispersive e_g^π - and a_{1g} -derived bands centered at the Γ and A points, respectively. The observed band structures were compared with the band-structure calculations based on DFT with GGA + U correction. Detailed analysis with varying U revealed that the obtained band structure is well-described by the DFT calculation at $U = 2.2$ eV. These results suggest that the electron–electron correlation plays an important role in describing the overall electronic structure of Ti_2O_3 . Nevertheless, the influence of electron–electron correlation on the quantum phase transition in Ti_2O_3 is considered to be weak owing to its low carrier density. Therefore, the ARPES and DFT calculation results presented here have important implications regarding the origin of the characteristic MIT in Ti_2O_3 ; the MIT is a semimetal–semimetal or semimetal–semiconductor transition caused by changes in the FS topology due to lattice deformation.

ACKNOWLEDGMENTS

The authors acknowledge R. Tokunaga, X. Cheng, and D. K. Nguyen for their support in the experiments at KEK-PF. The authors also thank R. Yukawa for sharing his program for analyzing ARPES data with us and for his assistance with data analysis. This work was financially supported by a Grant-in-Aid for Scientific Research (Nos. 16H02115, 16KK0107, 20KK0117, 22H01948, and 22H01947) from the Japan Society for the Promotion of Science

(JSPS), CREST (JPMJCR18T1) from the Japan Science and Technology Agency (JST), the MEXT Element Strategy Initiative to Form Core Research Center (JPMXP0112101001), Asahi Glass Foundation, Iketani Science and Technology Foundation, Nagamori Foundation, Research Foundation for the Electrotechnology of Chubu, and Toyota Riken Scholar Program. N.H. acknowledges financial support from the Chemistry Personnel Cultivation Program of the Japan Chemical Industry Association. T.K. acknowledges financial support from the Division for Interdisciplinary Advanced Research and Education at Tohoku University. The work performed at KEK-PF was approved by the Program Advisory Committee (proposals 2019T004, 2018S2-004, 2021G621, and 2021S2-002) at the Institute of Materials Structure Science, KEK. The authors would also like to thank Editage (www.editage.com) for English language editing.

References

1. J. M. Honig and T. B. Reed, "Electrical Properties of Ti_2O_3 Single Crystals" *Phys. Rev.* **174**, 1020 (1968). DOI: [10.1103/PhysRev.174.1020](https://doi.org/10.1103/PhysRev.174.1020).
2. J. M. Honig, "Nature of the Electrical Transition in Ti_2O_3 " *Rev. Mod. Phys.* **40**, 748 (1968). DOI: [10.1103/RevModPhys.40.748](https://doi.org/10.1103/RevModPhys.40.748).
3. J. J. Capponi, M. Marezio, J. Dumas, and C. Schlenker, "Lattice parameters variation with temperature of Ti_2O_3 and $(\text{Ti}_{0.98}\text{V}_{0.02})_2\text{O}_3$ from single crystal X-Ray data" *Solid State Commun.* **20**, 893 (1976). DOI: [10.1016/0038-1098\(76\)91299-0](https://doi.org/10.1016/0038-1098(76)91299-0).
4. C. N. R. Rao, R. E. Loehman, and J. M. Honig, "Crystallographic study of the transition in Ti_2O_3 " *Phys. Lett.* **27A**, 271 (1968). DOI: [10.1016/0375-9601\(68\)90696-8](https://doi.org/10.1016/0375-9601(68)90696-8).
5. L. L. Van Zandt, J. M. Honig, and J. B. Goodenough, "Resistivity and magnetic order in Ti_2O_3 " *J. Appl. Phys.* **39**, 594–595 (1968). DOI: [10.1063/1.2163536](https://doi.org/10.1063/1.2163536).
6. H. J. Zeiger, "Unified model of the insulator-metal transition in Ti_2O_3 and the high-temperature Transitions in V_2O_3 " *Phys. Rev. B* **11**, 5132 (1975). DOI: [10.1103/PhysRevB.11.5132](https://doi.org/10.1103/PhysRevB.11.5132).
7. M. Uchida, J. Fujioka, Y. Onose, and Y. Tokura, "Charge dynamics in thermally and doping induced insulator-metal transitions of $(\text{Ti}_{1-x}\text{V}_x)_2\text{O}_3$ " *Phys. Rev. Lett.* **101**, 066406 (2008). DOI: [10.1103/PhysRevLett.101.066406](https://doi.org/10.1103/PhysRevLett.101.066406).
8. C. F. Chang, T. C. Koethe, Z. Hu, J. Weinen, S. Agrestini, L. Zhao, J. Gegner, H. Ott, G. Panaccione, H. Wu, M. W. Haverkort, H. Roth, A. C. Komarek, F. Offi, G. Monaco, Y. –F. Liao, K. –D. Tsuei, H. –J. Lin, C. T. Chen, A. Tanaka, and L. H. Tjeng, "*c*-Axis Dimer and Its Electronic Breakup: The Insulator-to-Metal Transition in Ti_2O_3 " *Phys. Rev. X* **8**, 021004 (2018). DOI: [10.1103/PhysRevX.8.021004](https://doi.org/10.1103/PhysRevX.8.021004).
9. G. V. Chandrashekhar, Q. Won Choi, J. Moyo, and J. M. Honig, "The electrical transition in

- V-doped Ti₂O₃" Mater. Res. Bull. 5,999–1007(1970). DOI: [10.1016/0025-5408\(70\)90048-6](https://doi.org/10.1016/0025-5408(70)90048-6).
10. L. F. Mattheiss, "Electronic structure of rhombohedral Ti₂O₃" J. Phys.: Condens. Mater **8**, 5987 (1996). DOI: [10.1088/0953-8984/8/33/007](https://doi.org/10.1088/0953-8984/8/33/007).
 11. V. Singh and J. J. Pulikkotil, "Electronic phase transition and transport properties of Ti₂O₃" J. Alloys Compd. **658**, 430 (2016). DOI: [10.1016/j.jallcom.2015.10.203](https://doi.org/10.1016/j.jallcom.2015.10.203).
 12. Y. Tsujimoto, Y. Matsushita, S. Yu, K. Yamaura, T. Uchikoshi, "Size dependence of structural, magnetic, and electrical properties in corundum-type Ti₂O₃ nanoparticles showing insulator–metal transition" J. Asian Ceram. Soc. 3, 325–333 (2015). DOI: [10.1016/j.jascer.2015.06.007](https://doi.org/10.1016/j.jascer.2015.06.007).
 13. F. J. Morin, "Oxides which show a metal-to-insulator transition at the Neel temperature" Phys. Rev. Lett. **3**, 34 (1959). DOI: [10.1103/PhysRevLett.3.34](https://doi.org/10.1103/PhysRevLett.3.34).
 14. A. Tanaka, "On the metal-insulator transitions in VO₂ and Ti₂O₃ from a unified viewpoint" J. Phys. Soc. Jpn. **73**, 152 (2004). DOI: [10.1143/JPSJ.73.152](https://doi.org/10.1143/JPSJ.73.152).
 15. H. Sato, A. Tanaka, M. Sawada, F. Iga, K. Tsuji, M. Tsubota, M. Takemura, K. Yaji, M. Nagira, A. Kimura, T. Takabatake, H. Namatame, and M. Taniguchi, "Ti 3*d* orbital change across metal-insulator transition in Ti₂O₃: polarization-dependent soft x-ray absorption spectroscopy at Ti 2*p* edge" J. Phys. Soc. Jpn. **75**, 053702 (2006). DOI: [10.1143/JPSJ.75.053702](https://doi.org/10.1143/JPSJ.75.053702).
 16. K. Yoshimatsu, H. Kurokawa, K. Horiba, H. Kumigashira, and A. Ohtomo, "Large anisotropy in conductivity of Ti₂O₃ films" APL Mater. **6**, 101101 (2018). DOI: [10.1063/1.5050823](https://doi.org/10.1063/1.5050823).
 17. K. Yoshimatsu, N. Hasegawa, Y. Nambu, Y. Ishii, Y. Wakabayashi, and H. Kumigashira, "Metallic ground states of undoped Ti₂O₃ films induced by elongated *c*-axis lattice constant" Sci. Rep. **10**, 22109 (2020). DOI: [10.1038/s41598-020-79182-5](https://doi.org/10.1038/s41598-020-79182-5).
 18. Y. Guo, S. J. Clark, and J. Robertson, "Electronic and magnetic properties of Ti₂O₃, Cr₂O₃,

- and Fe_2O_3 calculated by the screened exchange hybrid density functional” J. Phys.: Condens. Mater **24**, 325504 (2012). DOI: [10.1088/0953-8984/24/32/325504](https://doi.org/10.1088/0953-8984/24/32/325504).
19. K. E. Smith and V. E. Henrich, “Bulk band dispersion in Ti_2O_3 and V_2O_3 ” Phys. Rev. B **38**, 5965 (1988). DOI: [10.1103/PhysRevB.38.5965](https://doi.org/10.1103/PhysRevB.38.5965).
 20. T. Uozumi, K. Okada, A. Kotani, Y. Tezuka, and S. Shin, “Ti $2p$ and resonant $3d$ photoemission spectra of Ti_2O_3 ” J. Phys. Soc. Jpn. **65**, 1150 (1996). DOI: [10.1143/jpsj.65.1150](https://doi.org/10.1143/jpsj.65.1150).
 21. J. M. McKay, M. H. Mohamed, and V. E. Henrich, “Localized $3p$ excitations in $3d$ transition-metal-series spectroscopy” Phys. Rev. B **35**, 4304 (1987). DOI: [10.1103/PhysRevB.35.4304](https://doi.org/10.1103/PhysRevB.35.4304).
 22. A. Mooradian and P. M. Raccach, “Raman study of the semiconductor-metal transition in Ti_2O_3 ” Phys. Rev. B **3**, 4253 (1971). DOI: [10.1103/PhysRevB.3.4253](https://doi.org/10.1103/PhysRevB.3.4253).
 23. S. A. Chambers, M. H. Engelhard, L. Wang, T. C. Droubay, M. E. Bowden, M. J. Wahila, N. F. Quackenbush, L. F. J. Piper, Tien-Lin Lee, C. J. Nelin, and P. S. Bagus, “X-ray photoelectron spectra for single-crystal Ti_2O_3 : Experiment and theory” Phys. Rev. B **96**, 205143 (2017). DOI: [10.1103/PhysRevB.96.205143](https://doi.org/10.1103/PhysRevB.96.205143).
 24. F. Iori, M. Gatti, and A. Rubio, “Role of nonlocal exchange in the electronic structure of correlated oxides” Phys. Rev. B **85**, 115129 (2012). DOI: [10.1103/PhysRevB.85.115129](https://doi.org/10.1103/PhysRevB.85.115129).
 25. A. I. Poteryaev, A. I. Lichtenstein, and G. Kotliar, “Nonlocal Coulomb interaction and metal-insulator transition in Ti_2O_3 : A cluster LDA + DMFT approach” Phys. Rev. Lett. **93**, 086401 (2004). DOI: [10.1103/PhysRevLett.93.086401](https://doi.org/10.1103/PhysRevLett.93.086401).
 26. H. Nakatsugawa and E. Iguchi, “Transition phenomenon in Ti_2O_3 using the discrete variational $X\alpha$ cluster method and periodic shell model” Phys. Rev. B **56**, 12931 (1997). DOI: [10.1103/PhysRevB.56.12931](https://doi.org/10.1103/PhysRevB.56.12931).

27. G. V. Chandrashekhar, Q. Won Choi, J. Moyo, and J. M. Honig, “The electrical transition in V-doped Ti_2O_3 ” *Mat. Res. Bull.* **5**, 999 (1970). DOI: [10.1016/0025-5408\(70\)90048-6](https://doi.org/10.1016/0025-5408(70)90048-6).
28. S. H. Shin, R. L. Aggarwal, B. Lax, and J. M. Honig, “Raman scattering in Ti_2O_3 - V_2O_3 alloys” *Phys. Rev. B* **9**, 583 (1974). DOI: [10.1103/PhysRevB.9.583](https://doi.org/10.1103/PhysRevB.9.583).
29. S. H. Shin, F. H. Pollak, T. Halpern, P. M. Raccach, “Resonance Raman scattering in Ti_2O_3 in the range 1.8–2.7 eV” *Solid State Commun.* **16**, 687 (1975). DOI: [10.1016/0038-1098\(75\)90453-6](https://doi.org/10.1016/0038-1098(75)90453-6).
30. A. Tanaka, “A New Scenario on the Metal–Insulator Transition in VO_2 ” *J. Phys. Soc. Jpn.* **72**, 2433–2436 (2003). DOI: [10.1143/JPSJ.72.2433](https://doi.org/10.1143/JPSJ.72.2433).
31. C. E. Rice and W. R. Robinson “Structural changes in the solid solution $(\text{Ti}_{1-x}\text{V}_x)_2\text{O}_3$ as a varies from zero to one” *J. Solid State Chem.* **21**, 145 (1977). DOI: [10.1016/0022-4596\(77\)90154-2](https://doi.org/10.1016/0022-4596(77)90154-2)
32. M. Imada, A. Fujimori, and Y. Tokura, “Metal-insulator transitions” *Rev. Mod. Phys.* **70**, 1039 (1998). DOI: [10.1103/RevModPhys.70.1039](https://doi.org/10.1103/RevModPhys.70.1039).
33. A. Damascelli, “Probing the Electronic Structure of Complex Systems by ARPES” *Phys. Scr.* **61**, T109 (2004). DOI: [10.1238/Physica.Topical.109a00061](https://doi.org/10.1238/Physica.Topical.109a00061).
34. A. Damascelli, Z. Hussain, and Z.-X. Shen, “Angle-resolved photoemission studies of the cuprate superconductors” *Rev. Mod. Phys.* **75**, 473 (2003). DOI: [10.1103/RevModPhys.75.473](https://doi.org/10.1103/RevModPhys.75.473).
35. J. A. Sobota, Y. He, and Z.-X. Shen, “Angle-resolved photoemission studies of quantum materials” *Rev. Mod. Phys.* **93**, 025006 (2021). DOI: [10.1103/RevModPhys.93.025006](https://doi.org/10.1103/RevModPhys.93.025006).
36. M. Kobayashi, K. Yoshimatsu, E. Sakai, M. Kitamura, K. Horiba, A. Fujimori, and H. Kumigashira, “Origin of the Anomalous Mass Renormalization in Metallic Quantum Well States of Strongly Correlated Oxide SrVO_3 ” *Phys. Rev. Lett.* **115**, 076801 (2015). DOI:

[10.1103/PhysRevLett.115.076801](https://doi.org/10.1103/PhysRevLett.115.076801).

37. M. Kobayashi, K. Yoshimatsu, T. Mitsuhashi, M. Kitamura, E. Sakai, R. Yukawa, M. Minohara, A. Fujimori, K. Horiba, and H. Kumigashira, “Emergence of Quantum Critical Behavior in Metallic Quantum-Well States of Strongly Correlated Oxides” *Sci. Rep.* **7**, 16621 (2017). DOI: [10.1038/s41598-017-16666-x](https://doi.org/10.1038/s41598-017-16666-x).
38. T. Mitsuhashi, M. Minohara, R. Yukawa, M. Kitamura, K. Horiba, M. Kobayashi, and H. Kumigashira, “Influence of k_{\perp} broadening on ARPES spectra of the (110) and (001) surfaces of SrVO₃ films” *Phys. Rev. B* **94**, 125148 (2016). DOI: [10.1103/PhysRevB.94.125148](https://doi.org/10.1103/PhysRevB.94.125148).
39. T. Kanda, D. Shiga, R. Yukawa, N. Hasegawa, D.K. Nguyen, X. Cheng, R. Tokunaga, M. Kitamura, K. Horiba, K. Yoshimatsu, and H. Kumigashira, “Electronic structure of SrTi_{1-x}V_xO₃ films studied by in situ photoemission spectroscopy: Screening for a transparent electrode material” *Phys. Rev. B* **104**, 115121 (2021). DOI: [10.1103/PhysRevB.104.115121](https://doi.org/10.1103/PhysRevB.104.115121).
40. R. Yukawa, M. Kobayashi, T. Kanda, D. Shiga, K. Yoshimatsu, S. Ishibashi, M. Minohara, M. Kitamura, K. Horiba, A. F. Santander-Syro, and H. Kumigashira, “Resonant tunneling driven metal-insulator transition in double quantum-well structures of strongly correlated oxide” *Nat. Commun.* **12**, 7070 (2021). DOI: [10.1038/s41467-021-27327-z](https://doi.org/10.1038/s41467-021-27327-z).
41. I. Lo Vecchio, J. D. Denlinger, O. Krupin, B. J. Kim, P. A. Metcalf, S. Lupi, J. W. Allen, and A. Lanzara, “Fermi surface of metallic V₂O₃ from angle-resolved photoemission: mid-level filling of e_g^{π} bands” *Phys. Rev. Lett.* **117**, 166401 (2016). DOI: [10.1103/PhysRevLett.117.166401](https://doi.org/10.1103/PhysRevLett.117.166401).
42. M. Thees, M. -H. Lee, R. L. Bouwmeester, P. H. Rezende-Gonçalves, E. David, A. Zimmers, F. Fortuna, E. Frantzeskakis, N. M. Vargas, Y. Kalcheim, P. Le Fèvre, K. Horiba, H. Kumigashira, S. Biermann, J. Trastoy, M. J. Rozenberg, I. K. Schuller, and A. F. Santander-Syro, “Imaging the itinerant-to-localized transmutation of electrons across the metal-to-

- insulator transition in V_2O_3 ” *Sci. Adv.* **7**, eabj1164 (2021). DOI: [10.1126/sciadv.abj1164](https://doi.org/10.1126/sciadv.abj1164).
43. F. Bisti, V. A. Rogalev, M. Karolak, S. Paul, A. Gupta, T. Schmitt, G. Güntherodt, V. Eyert, G. Sangiovanni, G. Profeta, and V. N. Strocov, “Weakly-correlated nature of ferromagnetism in nonsymmorphic CrO_2 revealed by bulk-sensitive soft-x-ray ARPES” *Phys. Rev. X* **7**, 041067 (2017). DOI: [10.1103/PhysRevX.7.041067](https://doi.org/10.1103/PhysRevX.7.041067).
44. V. N. Strocov, A. Chikina, M. Caputo, M. –A. Husanu, F. Bisti, D. Bracher, T. Schmitt, F. Miletto Granozio, C. A. F. Vaz, and F. Lechermann, “Electronic phase separation at $LaAlO_3/SrTiO_3$ interfaces tunable by oxygen deficiency” *Phys. Rev. Mater.* **3**, 106001 (2019). DOI: [10.1103/PhysRevMaterials.3.106001](https://doi.org/10.1103/PhysRevMaterials.3.106001).
45. A. Chikina, D. V. Christensen, V. Borisov, M. –A. Husanu, Y. Chen, X. Wang, T. Schmitt, M. Radovic, N. Nagaosa, A. S. Mishchenko, R. Valentí, and V. N. Strocov, “Band-order anomaly at the γ - $Al_2O_3/SrTiO_3$ interface drives the electron-mobility boost” *ACS Nano* **15**, 4347–4356 (2021). DOI: [10.1021/acsnano.0c07609](https://doi.org/10.1021/acsnano.0c07609).
46. V. N. Strocov, L. L. Lev, M. Kobayashi, C. Cancellieri, M. –A. Husanu, A. Chikina, N. B. M. Schröter, X. Wang, J. A. Krieger, and Z. Salman, “k-resolved electronic structure of buried heterostructure and impurity systems by soft-X-ray ARPES” *J. Electron Spectrosc. Relat. Phenom.* **236**, 1–8 (2019). DOI: [10.1016/j.elspec.2019.06.009](https://doi.org/10.1016/j.elspec.2019.06.009).
47. L. L. Lev, J. Krempaský, U. Staub, V. A. Rogalev, T. Schmitt, M. Shi, P. Blaha, A. S. Mishchenko, A. A. Veligzhanin, Y. V. Zubavichus, M. B. Tsetlin, H. Volfová, J. Braun, J. Minár, and V. N. Strocov, “Fermi surface of three-dimensional $La_{1-x}Sr_xMnO_3$ explored by soft-x-ray ARPES: Rhombohedral lattice distortion and its effect on magnetoresistance” *Phys. Rev. Lett.* **114**, 237601 (2015). DOI: [10.1103/PhysRevLett.114.237601](https://doi.org/10.1103/PhysRevLett.114.237601).
48. M. –A. Husanu, L. Vistoli, C. Verdi, A. Sander, V. Garcia, J. Rault, F. Bisti, L. L. Lev, T. Schmitt, F. Giustino, A. S. Mishchenko, M. Bibes, and V. N. Strocov, “Electron-polaron

- dichotomy of charge carriers in perovskite oxides” Commun. Phys. **3**, 62 (2020). DOI: [10.1038/s42005-020-0330-6](https://doi.org/10.1038/s42005-020-0330-6).
49. G. Berner, M. Sing, H. Fujiwara, A. Yasui, Y. Saitoh, A. Yamasaki, Y. Nishitani, A. Sekiyama, N. Pavlenko, T. Kopp, C. Richter, J. Mannhart, S. Suga, and R. Claessen, “Direct k -space mapping of the electronic structure in an oxide-oxide interface” Phys. Rev. Lett. **110**, 247601 (2013). DOI: [10.1103/PhysRevLett.110.247601](https://doi.org/10.1103/PhysRevLett.110.247601).
 50. See Supplemental Material at <http://link.aps.org/supplemental/XXXXXXXXXXXXXXXX> for preparation of TiO_x ceramic target, crystal structures of the films, transport properties of the films, band-structure calculations, and analysis details of the ARPES data.
 51. K. Yoshimatsu, O. Sakata, and A. Ohtomo, “Superconductivity in Ti₄O₇ and γ -Ti₃O₅ films” Sci. Rep. **7**, 12544 (2017). DOI: [10.1038/s41598-017-12815-4](https://doi.org/10.1038/s41598-017-12815-4).
 52. H. Kurokawa, K. Yoshimatsu, O. Sakata, and A. Ohtomo, “Effects of phase fraction on superconductivity of low-valence eutectic titanate films” J. Appl. Phys. **122**, 055302 (2017). DOI: [10.1063/1.4997443](https://doi.org/10.1063/1.4997443).
 53. P. Giannozzi, S. Baroni, N. Bonini, M. Calandra, R. Car, C. Cavazzoni, D. Ceresoli, G. L. Chiarotti, M. Cococcioni, I. Dabo, A. Dal Corso, S. de Gironcoli, S. Fabris, G. Fratesi, R. Gebauer, U. Gerstmann, C. Gougoussis, A. Kokalj, M. Lazzeri, L. Martin-Samos, N. Marzari, F. Mauri, R. Mazzarello, S. Paolini, A. Pasquarello, L. Paulatto, C. Sbraccia, S. Scandolo, G. Sclauzero, A. P. Seitsonen, A. Smogunov, P. Umari and R. M. Wentzcovitch, “QUANTUM ESPRESSO: a modular and open-source software project for quantum simulations of materials” J. Phys.: Condens. Matter **21**, 395502 (2009). DOI: [10.1088/0953-8984/21/39/395502](https://doi.org/10.1088/0953-8984/21/39/395502).
 54. P. Giannozzi, O. Andreussi, T. Brumme, O. Bunau, M. B. Nardelli, M. Calandra, R. Car, C. Cavazzoni, D. Ceresoli, M. Cococcioni, N. Colonna, I. Carnimeo, A. Dal Corso, S. de

- Gironcoli, P. Delugas, R. A. DiStasio, Jr., A. Ferretti, A. Floris, G. Fratesi, G. Fugallo, R. Gebauer, U. Gerstmann, F. Giustino, T. Gorni, J. Jia, M. Kawamura, H.-Y. Ko, A. Kokalj, E. Küçükbenli, M. Lazzeri, M. Marsili, N. Marzari, F. Mauri, N. L. Nguyen, H.-V. Nguyen, A. Otero-de-laRoza, L. Paulatto, S. Poncé, D. Rocca, R. Sabatini, B. Santra, M. Schlipf, A. P. Seitsonen, A. Smogunov, I. Timrov, T. Thonhauser, P. Umari, N. Vast, X. Wu and S. Baroni, “Advanced capabilities for materials modelling with Quantum ESPRESSO” *J. Phys.: Condens. Matter* **29**, 465901 (2017). DOI: [10.1088/1361-648X/aa8f79](https://doi.org/10.1088/1361-648X/aa8f79).
55. J. P. Perdew, K. Burke, and M. Ernzerhof, “Generalized gradient approximation made simple” *Phys. Rev. Lett.* **77**, 3865 (1996). DOI: [10.1103/PhysRevLett.77.3865](https://doi.org/10.1103/PhysRevLett.77.3865).
56. H. J. Monkhorst and J. D. Pack, “Special points for Brillouin-zone integrations” *Phys. Rev. B* **13**, 5188 (1976). DOI: [10.1103/PhysRevB.13.5188](https://doi.org/10.1103/PhysRevB.13.5188).
57. S. Hüfner, “Photoelectron Spectroscopy” (Springer-Verlag, Berlin,1995). ISBN: [978-3-662-03150-6](https://www.springer.com/9783662031506)
58. G. Levy, W. Nettker, B. M. Ludbrook, C. N. Veenstra, and A. Damascelli, “Deconstruction of resolution effects in angle-resolved photoemission” *Phys. Rev. B* **90**, 045150 (2014). DOI: [10.1103/PhysRevB.90.045150](https://doi.org/10.1103/PhysRevB.90.045150).

Supplemental Material

Electronic band structure of Ti_2O_3 thin films studied by angle-resolved photoemission spectroscopy

Naoto Hasegawa¹, Kohei Yoshimatsu^{1,2,*}, Daisuke Shiga¹, Tatsuhiko Kanda¹, Satoru Miyazaki¹, Miho Kitamura³, Koji Horiba³, and Hiroshi Kumigashira^{1,2,3}

¹ *Institute of Multidisciplinary Research for Advanced Materials (IMRAM), Tohoku University, Sendai, 980–8577, Japan*

² *Materials Research Center for Element Strategy (MCES), Tokyo Institute of Technology, Yokohama 226–8503, Japan*

³ *Photon Factory, Institute of Materials Structure Science, High Energy Accelerator Research Organization (KEK), Tsukuba, 305–0801, Japan*

*Correspondence: kohei.yoshimatsu.c6@tohoku.ac.jp

1. Sample growth and characterization

1.1 Preparation of Ti₂O₃ ceramic target

A ceramic target for laser ablation with a nominal composition of Ti₂O₃ was prepared using a solid-state reaction method. Ti (3N purity) and TiO₂ (4N purity) powders with a molar ratio of 1:3 were mixed and then pelletized. The pellet was sintered at 1100°C for 12 h with continuous Ar/H₂ gas flow (0.5 L/min) to achieve a highly reductive atmosphere in which the Ti₂O₃ phase could be stabilized.

1.2 Crystal structure of Ti₂O₃ films

Figure S1(a) shows the out-of-plane X-ray diffraction (XRD) pattern of the Ti₂O₃ films on α -Al₂O₃ (0001) substrates. Two film-derived peaks were detected at 2θ of approximately 39.12° and 84.10°, corresponding to the Ti₂O₃ 0006 and 00012 reflections, respectively. From the reflections, the c -axis lattice constant was estimated to be 13.80 Å. The full width at half maximum of the Ti₂O₃ 0006 reflection is 0.057° in the ω -scan rocking curve profile (inset of Fig. S1(a)), confirming the high crystallinity of the obtained films.

The a -axis lattice constant of the Ti₂O₃ films was determined from the reciprocal space map shown in Fig. S1(b). The a -axis lattice constant was estimated to be 5.102 Å from the Ti₂O₃ 10-110 reciprocal point, and thus, the c/a ratio is 2.70. The c/a ratio is larger than that of Ti₂O₃ bulk single crystals ($c/a = 2.639$ from $a = 5.157$ Å and $c = 13.61$ Å) [3]. Note that the obtained lattice constants are almost identical to those in previous reports [16,17], where the films were grown under almost the same conditions. In the present ARPES analyses and density functional theory (DFT) calculations, we adopted the experimentally determined lattice parameters ($a = 5.102$ Å, $c = 13.80$ Å, and $c/a = 2.70$).

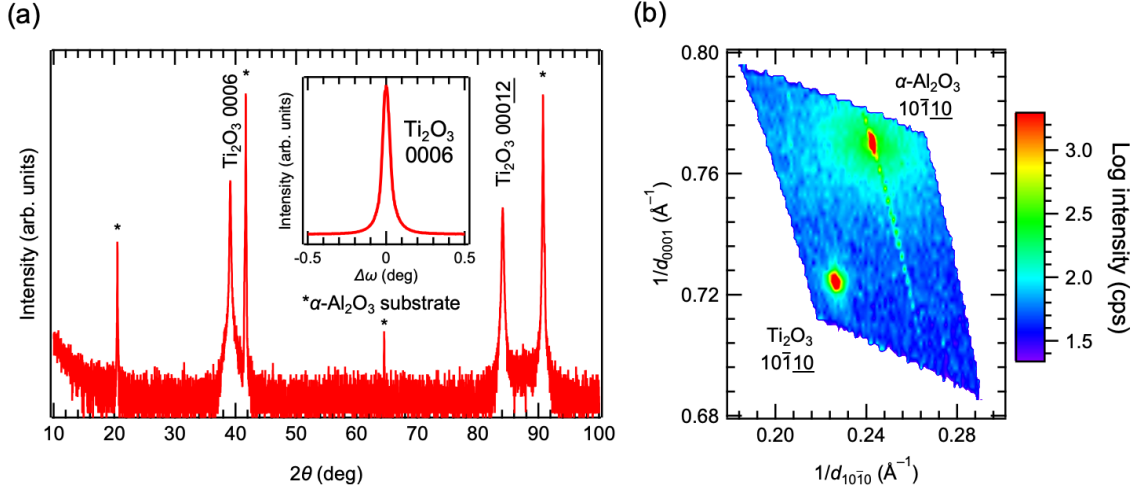


FIG. S1. (a) Out-of-plane XRD pattern of the Ti_2O_3 films grown on $\alpha\text{-Al}_2\text{O}_3$ (0001) substrates. The inset shows the ω -scan rocking curve profile of the Ti_2O_3 0006 reflection. (b) Reciprocal space map of the Ti_2O_3 films around the $\alpha\text{-Al}_2\text{O}_3$ $10\bar{1}10$ reciprocal point.

1.3 Transport properties of Ti_2O_3 films

Figure S2 shows the temperature dependence of the resistivity (ρ - T) for the Ti_2O_3 films. The ρ - T curves of the Ti_2O_3 bulk single crystals [7] and previously reported Ti_2O_3 films [16] are also shown for comparison. The present Ti_2O_3 films showed a broad metal-insulator transition (MIT) at approximately 250 K, accompanied by an order of magnitude change in resistivity. The characteristic ρ - T curve around the MIT temperature (T_{MIT}) is in good agreement with that of previously reported Ti_2O_3 films with a hole concentration of $1.1 \times 10^{20} \text{ cm}^{-3}$ [16]. The T_{MIT} of approximately 250 K for the films is much lower than that for the bulk Ti_2O_3 (approximately 450 K) [2–9]. The lowering of T_{MIT} may originate from the large c/a ratio in the films [17].

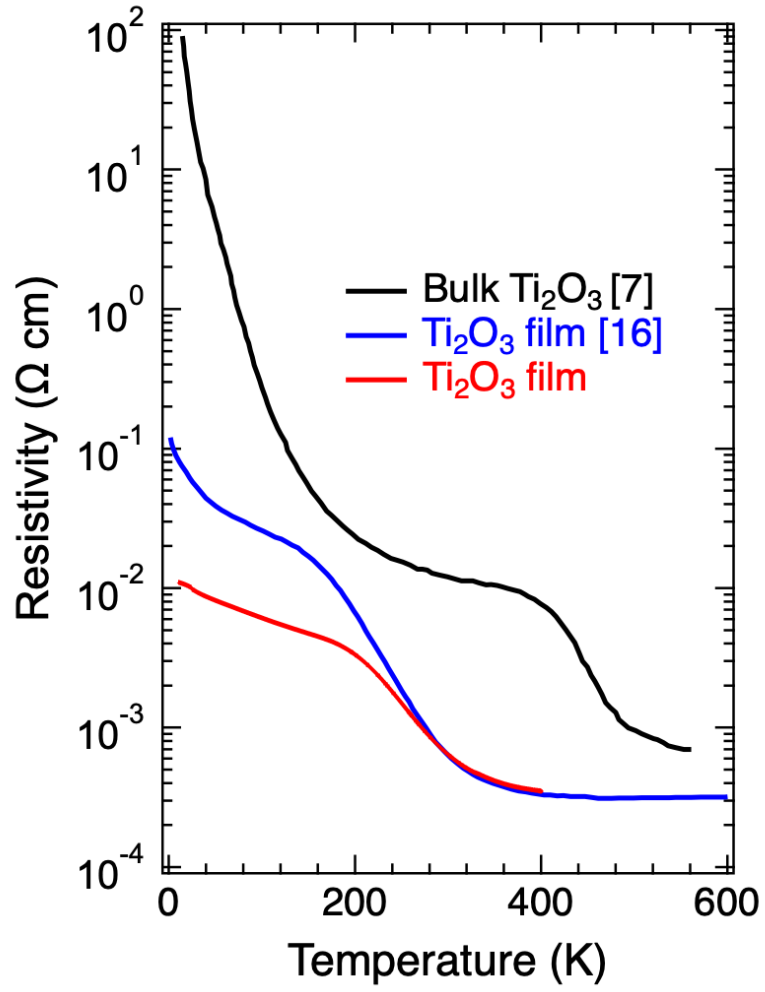


FIG. S2. Temperature dependence of resistivity ($\rho-T$) for the present Ti₂O₃ films. The $\rho-T$ curves of the Ti₂O₃ bulk single crystals [7] and previously reported Ti₂O₃ films [16] are also shown for comparison.

2. Band structure calculations based on DFT + U

2.1 DFT calculation details

Band-structure calculations based on DFT were conducted using the QUANTUM ESPRESSO software [53, 54]. The Perdew–Burke–Ernzerhof generalized gradient approximation (PBE-GGA) was adopted for the exchange–correlation functional [55]. The electron–ion interactions were described by ultrasoft pseudopotentials wherein atomic Ti $3s$, $3p$, $3d$, and $4s$ and O $2s$ and $2p$ levels were included in a valence-band state. The kinetic energy (charge density) cut-off was set to 60 (600) Ry.

The Ti and O atomic positions were optimized by the Monkhorst–Pack scheme using a $6 \times 6 \times 6$ k -point grid in a self-consistent scheme. In the self-consistent calculation, the lattice constants were fixed as the experimental values ($a = 5.102 \text{ \AA}$, $c = 13.80 \text{ \AA}$; see Fig. S1). After convergence of the self-consistent calculation, the accuracy of the total energy reached less than 10^{-10} Ry. We then conducted a non-self-consistent calculation to draw the band dispersion using 20 k points along each line. The DFT calculations were performed on the rhombohedral primitive Ti_2O_3 to reduce the computational cost. Thus, the band dispersion with the notation of the hexagonal Brillouin zone (BZ) was depicted by converting the rhombohedral BZ into an equivalent hexagonally shaped one [see Fig. 2(b)].

2.2 Possible magnetic ground states in Ti_2O_3 under a DFT + U approximation

The possible magnetic ground states of Ti_2O_3 were estimated from DFT + U calculations. Here, the calculations were performed assuming non-magnetic [corresponding to paramagnetic (PM)], antiferromagnetic (AFM), and ferromagnetic (FM) ground states while fixing the lattice parameters ($c/a = 2.70$) and U value ($U = 2.2 \text{ eV}$). The results are summarized in Table S1. The AFM states were most stable in Ti_2O_3 , which indicates that the AFM ground state is predicted in Ti_2O_3 within the framework of the DFT + U approximation. The local moment of Ti ions was $\pm 0.43 \mu_{\text{B}}/\text{Ti}$ in the AFM states and $1.00 \mu_{\text{B}}/\text{Ti}$ in the most unstable FM states. The total energy difference between the PM and AFM states in Ti_2O_3 is considerably smaller than that between the AFM and FM states. Therefore, we have adopted the calculations for the PM ground states in Ti_2O_3 on the basis of the experimental fact [1].

Table S1. Local magnetic moment and difference in total energy relative to the ground state for paramagnetic (PM), ferromagnetic (FM), and antiferromagnetic (AFM) Ti_2O_3 with $c/a = 2.70$ obtained from the DFT + U calculation ($U = 2.2$ eV).

	Moment (μ_B / Ti)	$E - E_{\text{AFM}}$ (kJ/mol)
PM	–	1.05
FM	1.00	11.68
AFM	± 0.43	–

2.3 Band structure of Ti_2O_3 obtained by DFT + U calculations

Figure S3 shows the calculated band structures of Ti_2O_3 based on the GGA+ U approximation. The experimentally determined lattice constants ($c/a = 2.70$) were used in the DFT calculations. Here, we present the results for the on-site Coulomb interaction parameter U of 0 eV and 2.2 eV, and the band dispersion along representative directions (Γ –K and A–H) are used in Fig. 4, where the Fermi level (E_F) is shifted toward higher-binding-energy side by 150 (180 meV) to reproduce the experimental results on the hole-doped Ti_2O_3 films for $U = 0$ eV (2.2 eV). As can be seen in Fig. S3 (also see the corresponding orbital projected band structures in Fig. S4), the Ti $3d$ -derived bands near E_F are mainly classified into two groups based on their dispersive features, reflecting the anisotropic shape of Ti $3d$ orbitals. One is the a_{1g} -derived band that is highly dispersive along the Γ –A direction (the out-of-plane direction in the present study) but less dispersive along the Γ –K direction (in-plane direction). The other is the e_g^π -derived band that shows less dispersive features along the out-of-plane direction but are highly dispersive along the in-plane directions. Meanwhile, the dispersive features along the A–H direction originate from the strong hybridization between the a_{1g} states and e_g^π and e_g^σ states. The e_g^π -derived band forms an electron pocket(s) at the Γ point, while the a_{1g} -derived band forms a hole pocket(s) at the A point for $U = 0$ eV or at the midpoint of the Γ –A line for $U = 2.2$ eV. The slight overlap between the two pockets makes intrinsic Ti_2O_3 a compensated semimetal.

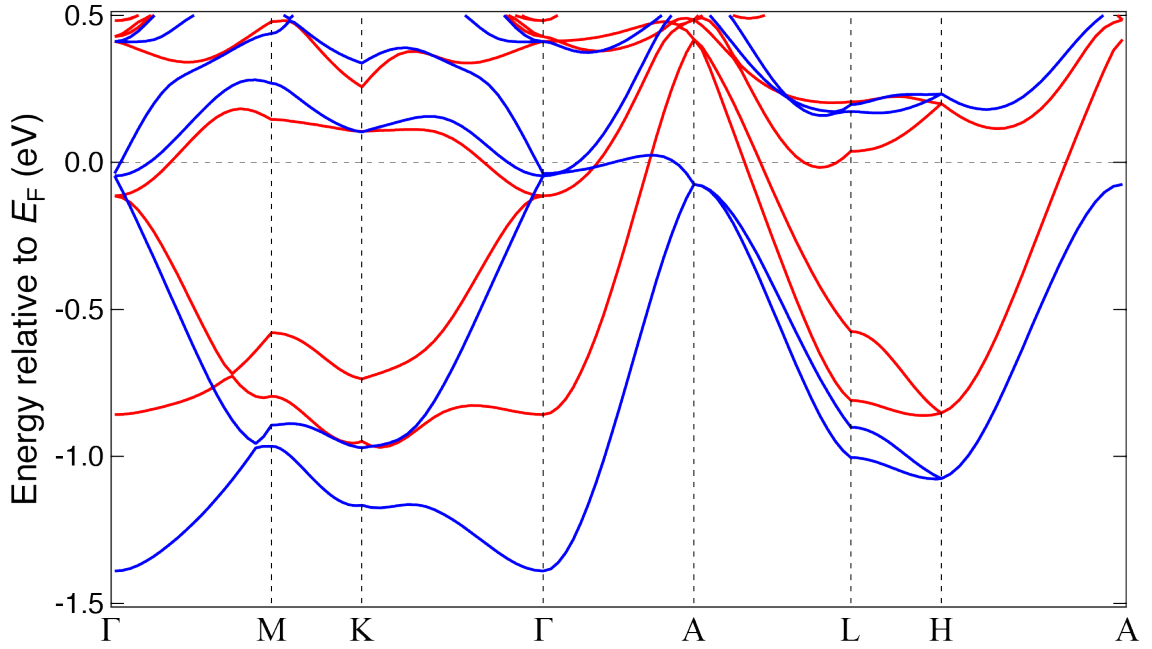


FIG. S3. Band structure of Ti₂O₃ obtained by the DFT + U calculations. The results for $U = 0$ and 2.2 eV are given as red and blue lines, respectively.

2.4 Orbital projected band dispersions of Ti₂O₃

Figure S4 shows the orbital projected band dispersions of Ti₂O₃ obtained from the DFT + U calculation with parameters of $c/a = 2.70$ and $U = 2.2$ eV. Note that the band dispersion itself is the same as that shown in Fig. S3. As can be seen in Fig. S4, the band structures around E_F consist of the e_g^π - and a_{1g} -derived states. Note that the results on the orbital projection are almost similar to those previously reported [10].

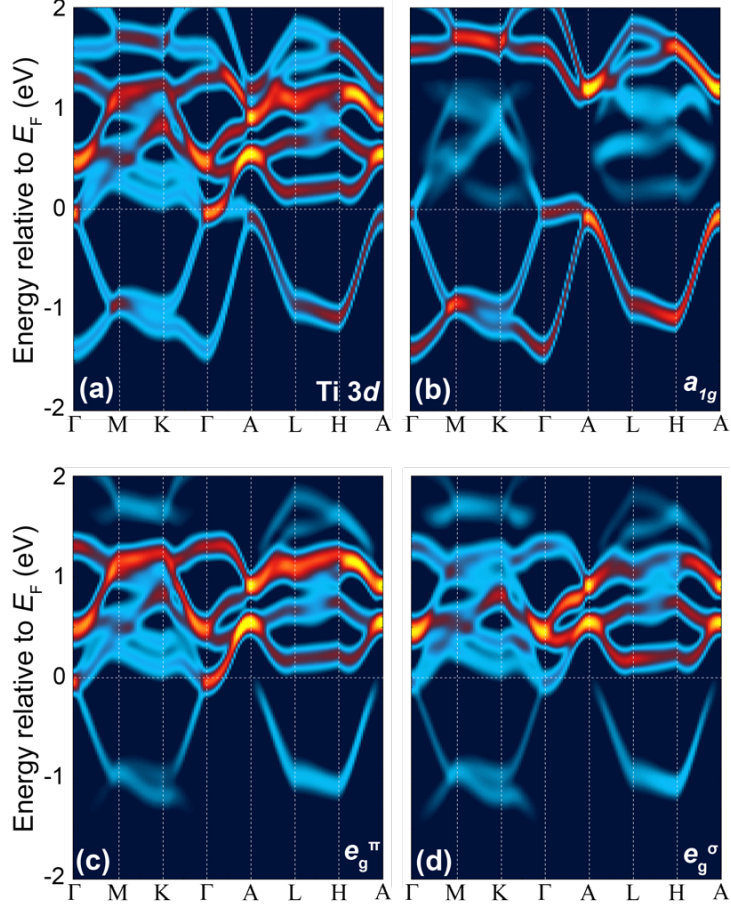


FIG. S4. The Ti 3d orbital contribution in the band structures of Ti_2O_3 calculated by the DFT + U method with $c/a = 2.70$ and $U = 2.2$ eV. The contributions of the total Ti 3d (a), a_{1g} (b), e_g^π (c), and e_g^σ (d) components for the band structures are plotted by color scale.

2.5 U dependence of the Ti_2O_3 band structure

Figure S5 shows the U dependence of the band structure of Ti_2O_3 with a fixed c/a ratio of 2.70. As shown in Fig. S5, Ti_2O_3 exhibits a transition from semimetal to semiconductor. With increasing U , the energy separation between the a_{1g} and e_g^π states becomes large; the a_{1g} -derived band is pushed down, whereas the e_g^π -derived band is pushed up. As a result, the electron and hole pockets at the Γ and A points simultaneously become smaller, and eventually a tiny energy gap opens at $U \geq 2.5$ eV. Accordingly, the occupancy of the lowest-lying a_{1g} state increases with increasing U . It is also worth noting that the increment of U causes narrowing of the a_{1g} -derived band dispersion along the A–H direction and widening of the e_g^π -derived band dispersion

along the Γ –K direction. Therefore, the bandwidth is a good indicator of the validity of the U value.

The semimetallic ground states of Ti_2O_3 for $U = 0$ – 2.2 eV originate from the slight overlap in energy between the e_g^π - and a_{1g} -derived bands near E_F . The increment of U initially appears to reduce the overlapping. However, a closer inspection of the Fermi surface (FS) reveals a significant change in the FS topology. In the range of $U = 0$ – 2.0 eV, the electron pocket at the Γ point and hole pocket at the A point make Ti_2O_3 a semimetal. However, for $U = 2.2$ eV, the electron pockets are formed at both the Γ and A points and are compensated by the hole pocket at the midpoint of the Γ –A line. The results suggest a delicate balance between the energy of the e_g^π and a_{1g} states causes a change in the FS topology of Ti_2O_3 and consequently a significant change in the character of the conduction carriers.

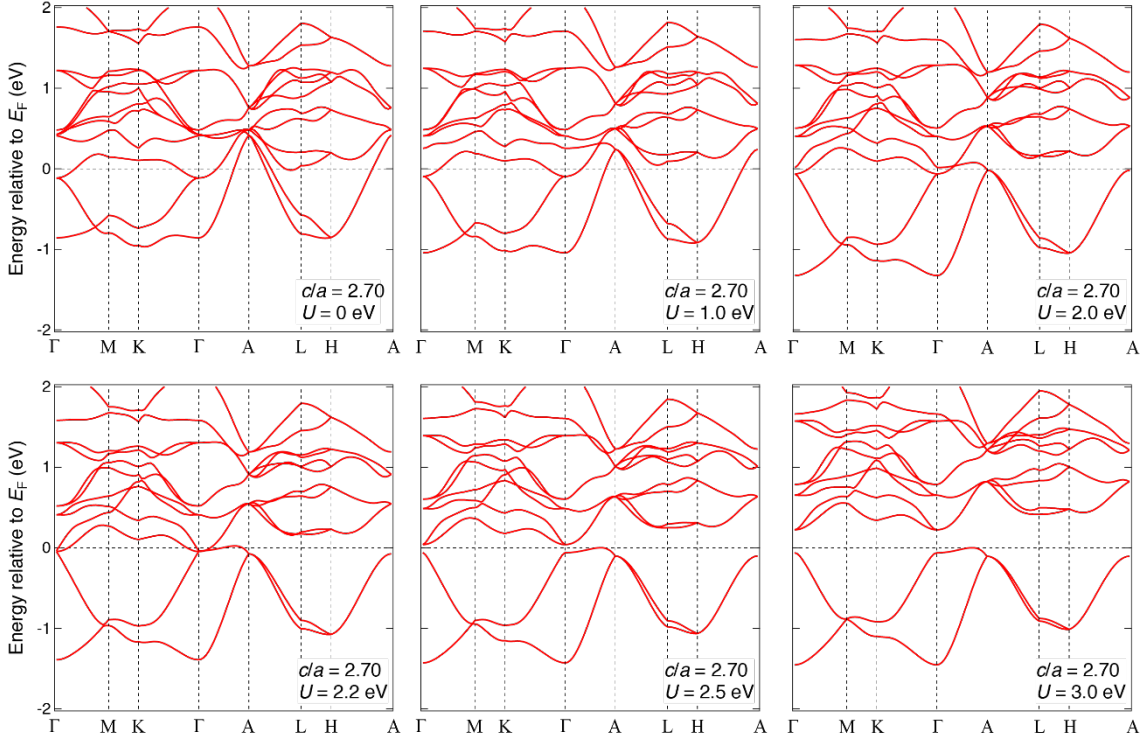


FIG. S5. Band structure of Ti_2O_3 with a c/a ratio of 2.70 calculated based on the GGA + U approximation. U is varied from 0 to 3.0 eV. Note that the results for $U = 0$ and 2.2 eV are the same as those in Fig. S3.

2.6 U dependence of the band structure of Ti_2O_3 with a c/a ratio of 2.639

Figure S6 shows the U dependence of the band structure of Ti_2O_3 with a fixed c/a ratio of 2.639 by varying U from 0 to 3.0 eV. The overall band structures and their U dependence are quite similar to those of Ti_2O_3 with a c/a ratio of 2.70 (see Fig. S5). A crucial difference is the critical U value for the MIT. In Ti_2O_3 with the c/a ratio of 2.639, the MIT occurs at the critical U value of 2.0 eV, whereas Ti_2O_3 with the c/a ratio of 2.70 exhibited the MIT at the critical U value of 2.5 eV (see Fig. S5). This difference in the critical U values suggests that the electronic structures of Ti_2O_3 also strongly depend on lattice deformation, as shown in Fig. S7.

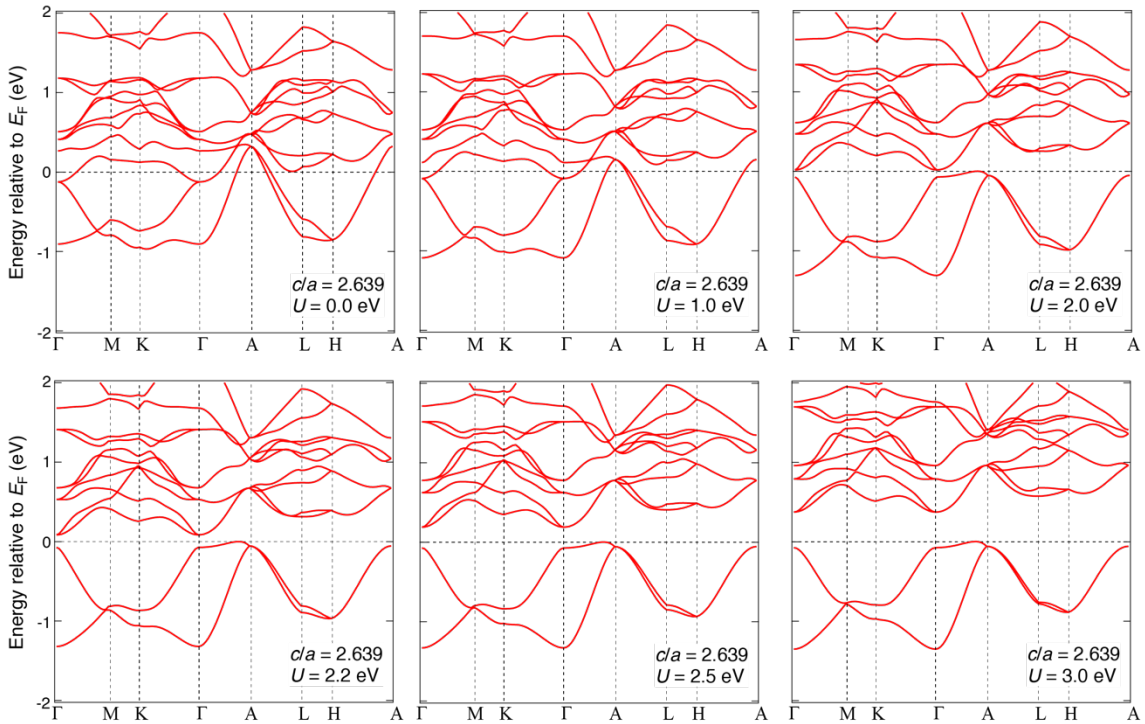


FIG. S6. Band structures of Ti_2O_3 with a c/a ratio of 2.639 calculated based on the GGA + U approximation. U is varied from 0 to 3.0 eV.

2.7 c/a ratio dependence of the Ti_2O_3 band structure

To investigate the effect of lattice deformation on the electronic band structure of Ti_2O_3 , band-structure calculations were conducted by varying the c/a ratio while keeping the U value fixed to 2.2 eV. Figure S7 shows the obtained c/a -ratio dependence of the band structure of Ti_2O_3 . With increasing the c/a ratio, the energy separation between the a_{1g} and e_g^π states becomes smaller; the a_{1g} -derived band is pushed up, whereas the e_g^π -derived band is pushed down. As a result, electron pockets appear at the Γ point, and simultaneously, a hole pocket appears at the midpoint of the Γ -A line for a critical c/a ratio of 2.68. The semimetallic ground states of Ti_2O_3 for $c/a \geq 2.68$ originate from the slight overlap in energy between the e_g^π - and a_{1g} -derived bands near E_F . Interestingly, the c/a -ratio dependence of these band structures (with increasing c/a) appears to be similar to the U dependence (with decreasing U) as shown in Figs. S5 and S6. These results demonstrate that the band structures of Ti_2O_3 strongly depend on both the parameters of the c/a ratio and U . Furthermore, the resultant delicate balance between the energy of the e_g^π and a_{1g} states causes a change in the FS topology of Ti_2O_3 , and consequently, a significant change in the character of the conduction carriers.

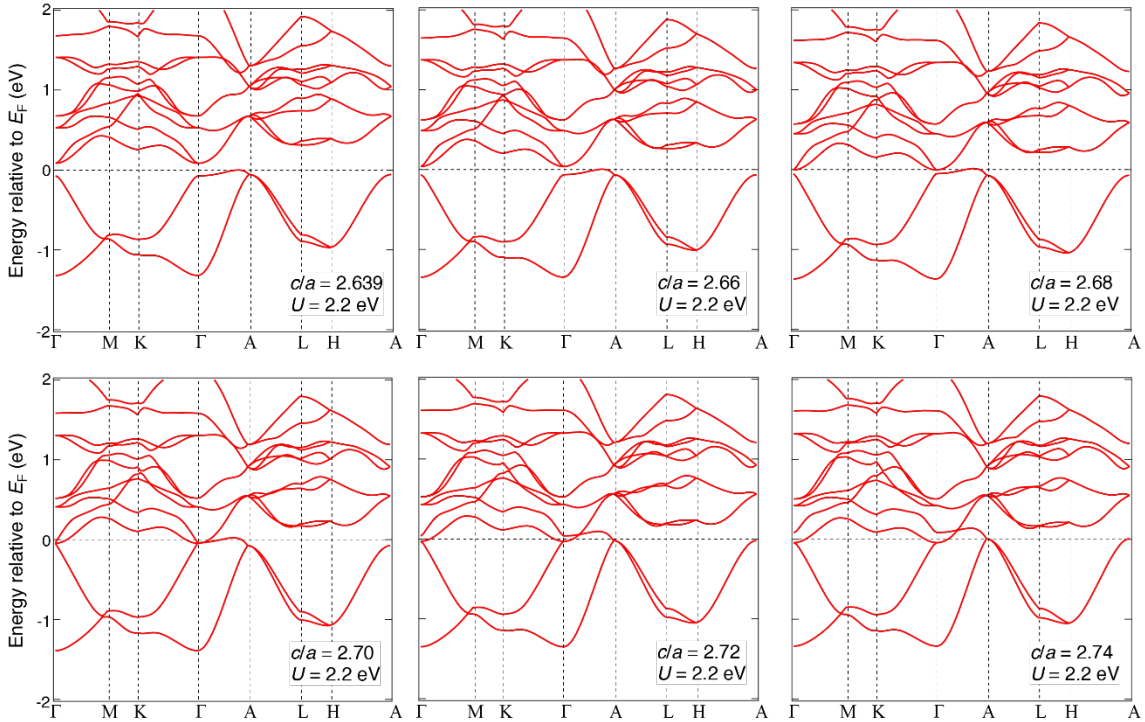


FIG. S7. Band structure of Ti_2O_3 calculated with a fixed U value of 2.2 eV based on the GGA + U approximation. The c/a ratio is varied from 2.639 to 2.74.

2.8 Fermi surface of Ti_2O_3

Figure S8 shows the Fermi surface (FS) of Ti_2O_3 corresponding to the band-structure calculation shown in Figs. 3 and 4 ($c/a = 2.70$ and $U = 2.2$ eV). Here, the Fermi level is shifted toward the higher-binding-energy-side for comparison with the ARPES results on the hole-doped Ti_2O_3 films, which is discussed in the main text. The cross-sectional FSs in the Γ -A-H-K plane [Fig. S8(b)], Γ -K-M plane [Fig. S8(c)], and A-H-L plane [Fig. S8(d)] are shown for comparison with the ARPES results. As shown in Fig. S9, the FSs determined by ARPES are well reproduced by the DFT + U calculation, demonstrating that the determination of $U = 2.2$ eV is reasonable to reproduce the electronic structures of Ti_2O_3 in the framework of the present DFT + U approximation.

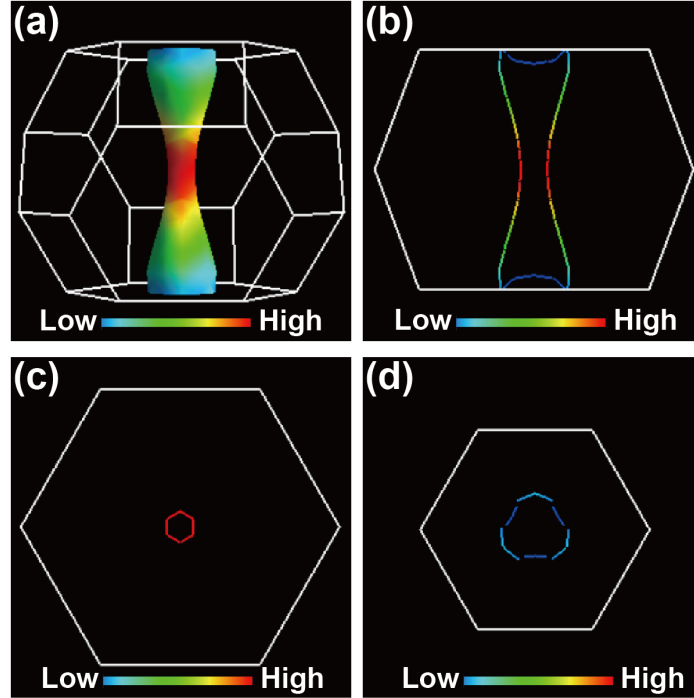


FIG. S8. (a) Fermi surfaces of Ti_2O_3 obtained from the DFT + U calculation ($c/a = 2.70$, $U = 2.2$ eV). The white lines indicate the first BZ of rhombohedral Ti_2O_3 . For comparison with the ARPES results, the Fermi level is shifted toward the higher-binding-energy side as in the same manner described in the text. (b–d) Fermi surfaces cut at representative planes. (b), (c), and (d) correspond to the Γ -A-H-K, Γ -K-M, and A-H-L planes in the hexagonally-shaped BZ of Ti_2O_3 , respectively. The weight of the Ti 3d components for the FS is shown by color scale. The FSs are visualized using the FermiSurfer software [S1].

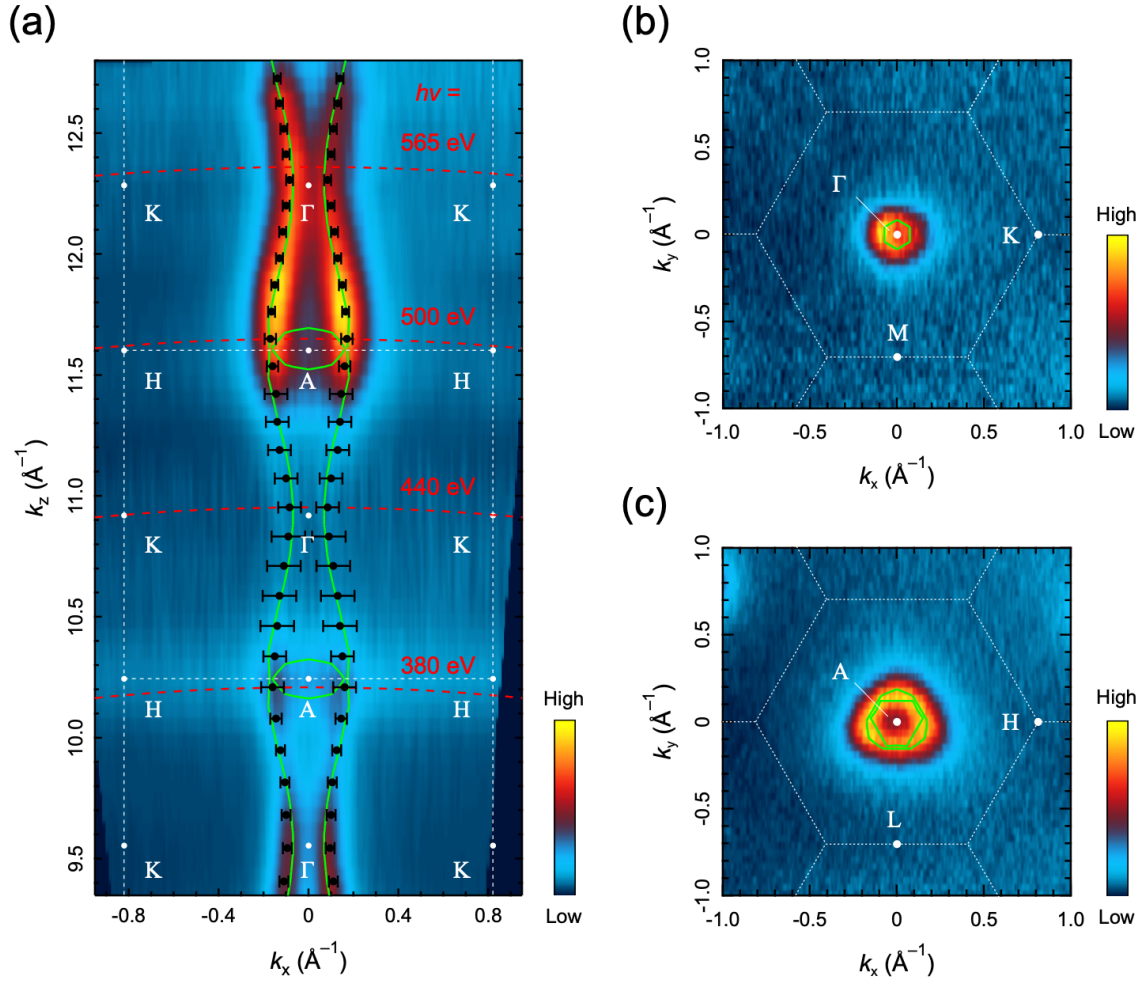


FIG. S9. Comparison of the Fermi surfaces between the ARPES results and DFT + U calculations on the Γ -A-H-K (a), Γ -K-M (b), and A-H-L (c) planes in the hexagonally-shaped BZ of Ti_2O_3 . The excellent agreement indicates the essential validity of our band-structure calculation (indicated by green lines) and ARPES analysis procedures.

2.9 Benchmark for evaluating the appropriate U value

As described in the text, we used $U = 2.2$ eV in the DFT + U calculation for comparison with the experimental results (Figs. 3 and 4). This is because the DFT calculation with $U = 2.2$ eV well reproduced the insulating phase of *bulk* Ti_2O_3 , which exhibits a small energy gap of approximately 100 meV at a c/a ratio of 2.639 [17]. The present DFT + U calculation with $U = 2.2$ eV well reproduces the energy gap in *bulk* Ti_2O_3 (see Figs. S6 and S7). The application of the same U value to the films is reasonable because the on-site Coulomb repulsion is not sensitive to changes in the environment of Ti ions owing to the narrow spatial distribution of Ti $3d$ electrons. Therefore, in our calculation for the Ti_2O_3 *films* shown in Figs. 3 and 4 (also Figs. S3–S5, S8, and S9), we used $U = 2.2$ eV and the c/a ratio of 2.70, which was determined from X-ray diffraction measurements at room temperature (see the reciprocal space map in Fig. S1). The suitability of the parameters is confirmed by the fact that the ARPES results are well reproduced by the calculation, especially the Fermi momentum k_F (Fig. 4) and FS topology (Fig. S9).

To further confirm the validity of $U = 2.2$ eV, we evaluated the suitability of the U value as follow. When U is not uniquely determined by comparing the band dispersion, as in the present case, the criterion for determining the appropriate U is the agreement in the k_F values between the DFT + U calculations and ARPES results. Thus, we utilized the k_F value in the same manner as described in the manuscript. We shifted the Fermi level in the DFT + U calculations with different U values (Fig. S5) by ΔE toward the higher-binding-energy side to reproduce the k_F at the Γ point, reflecting the hole-doped nature of the Ti_2O_3 films. Next, we judged the validity of U by evaluating the agreement of the k_F at the A point.

Figure S10 shows a series of the comparison between the experimental band structure and DFT + U calculations with different U values. In the plot for the difference in the k_F at the A point between the ARPES results and DFT + U calculations (Fig. S11), it is clear that the best match is obtained when $U = 2.2$ eV, although appropriate U values seem to be in the range of $U = 2.2$ – 2.4 eV by considering the experimental error. Based on the evaluation, we conclude that $U = 2.2$ eV is the most appropriate value for describing the band structure of Ti_2O_3 thin films.

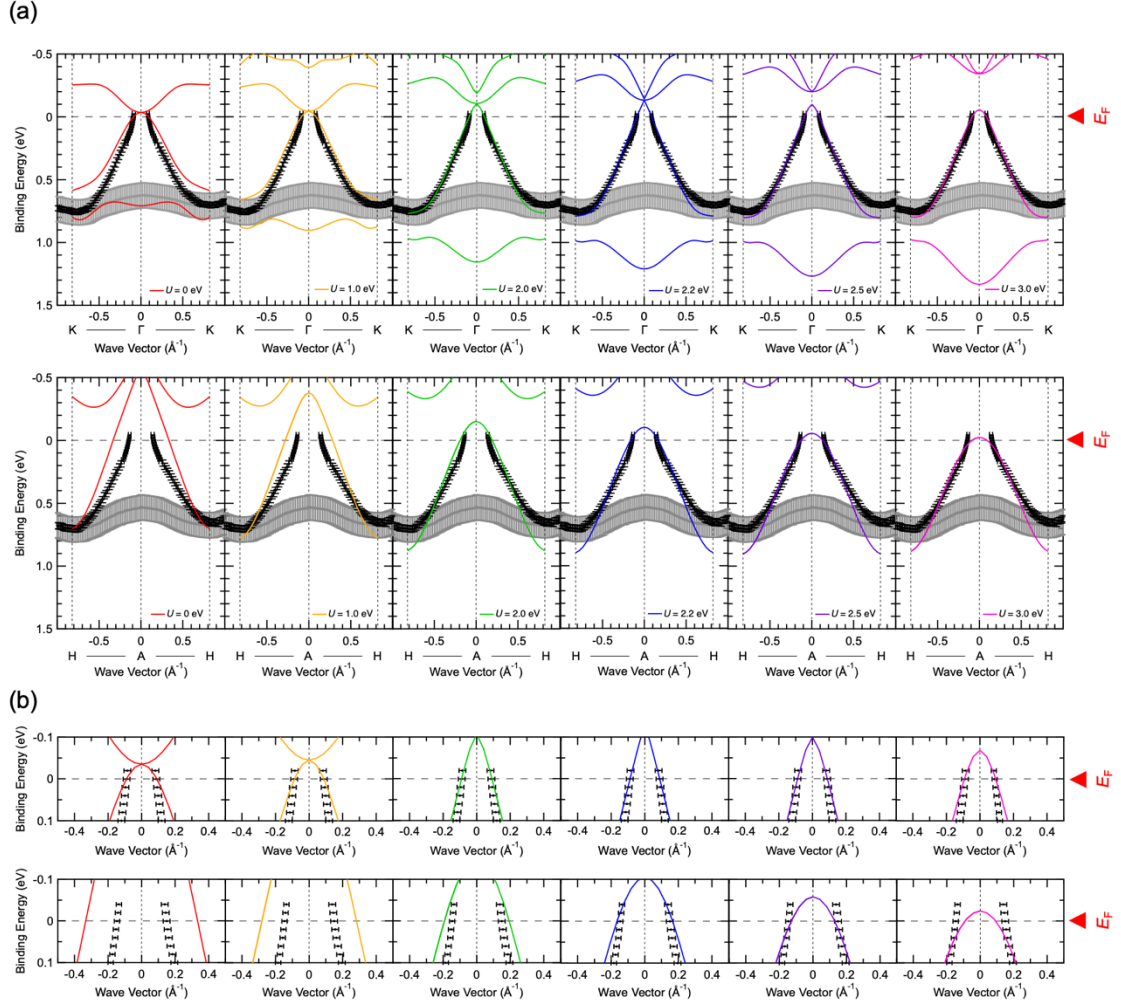


FIG. S10. Comparison of the experimental band structure and DFT + U calculation (a) in the energy range from 1.5 to -0.5 eV and (b) in the magnified scale near E_F along the Γ -K (upper panels) and A-H (lower panels) directions. The U value is varied from 0 to 3.0 eV with a constant c/a ratio of 2.70. The data markers indicate the Ti 3d bands determined by ARPES (same as those in Fig. 4), while the colored lines correspond to the results of the DFT + U calculations. The DFT + U results with $U = 0$ and 2.2 eV are the same as those used in Fig. 4. Note that the Fermi level in the DFT + U calculations is shifted toward the higher-binding-energy side to reproduce the k_F at the Γ point. It is evident that the best match is obtained at $U = 2.2$ eV.

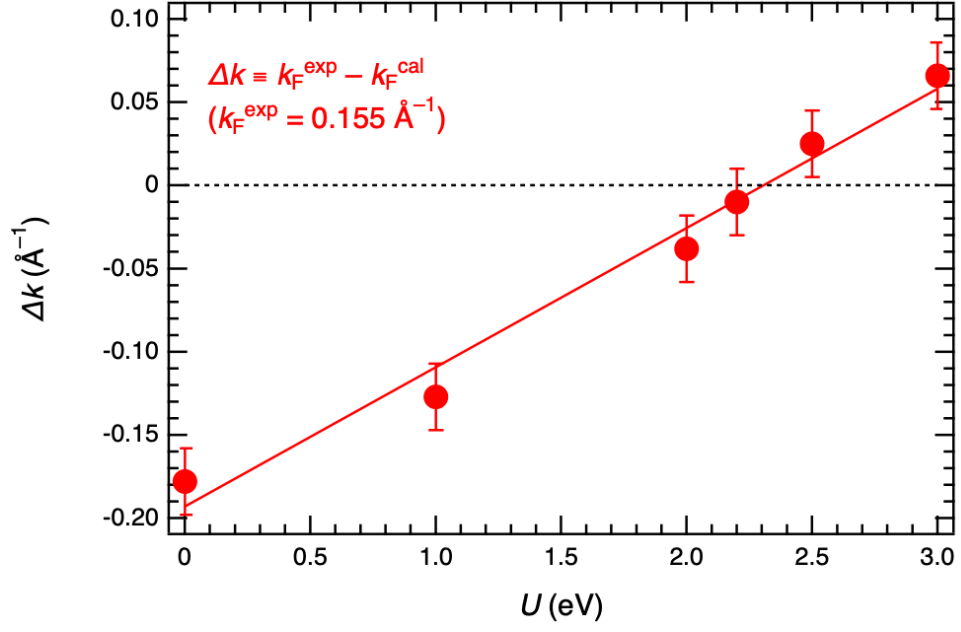


FIG. S11. Plot of differences in the k_F (Δk) between the ARPES experiments (k_F^{exp}) and DFT + U calculations (k_F^{cal}) at the A point as a function of U .

3. Analysis details of ARPES data

3.1 Out-of-plane FS mapping

Figure S12(a) shows the out-of-plane FS map of the Ti_2O_3 films obtained from normal-emission ARPES measurements in the Γ -A-H-K emission plane. Normal-emission (photon-energy dependent) ARPES images were taken along the k_x slice with changing the photon energy ($h\nu$) from 300 to 600 eV in 10 eV increments. Reflecting the hole-doped nature of the films, a meandering FS that follows the periodicity of the bulk BZ is clearly observed along the BZ center line. The cross-section of the FS is largest at the A points (corresponding to $h\nu = 500$ and 380 eV), monotonically decreases away from the A points, and is smallest at the Γ points (corresponding to $h\nu = 560$ and 440 eV). From this periodicity, the inner potential was determined to be approximately 21.8 eV.

3.2 Band dispersion along the Γ -A direction

Figure S12(b) shows the ARPES image along the Γ -A direction, which is drawn by picking up the normal-emission ARPES spectra from the photon-energy dependent ARPES images. A series of the normal-emission ARPES spectra is shown in Fig. S12(c). As can be seen in Fig. S12(b), some flat bands are only dimly observed in the ARPES image; broad and nondispersive quasi-localized states are located at approximately 0.6 eV, while flat states are located just below E_F for the bottom and top Γ points. The former may originate from the surface-derived states characteristic of corundum-type conductive oxides [42], while the latter may originate from the angle-integrated effects of the hole band that forms a closed hole surface in the proximity of the zone center line [see Fig. S12(a)]. However, a closer inspection in the energy range of 460–500 eV reveals the existence of a highly dispersive feature near E_F , which approaches E_F with increasing photon energy and may cross E_F around the A point, suggesting the formation of an additional small hole FS around the A point. In comparison with the DFT calculation [10] (also see Fig. S4), the dispersive band is attributable to the a_{1g} -derived band, which disperses highly along the Γ -A direction (out-of-plane direction), reflecting the anisotropic shape of the a_{1g} orbital. Meanwhile, the bottom of the band around the Γ point is unclear owing to the overlap with the surface-derived nondispersive quasi-localized states and certain matrix-element effects.

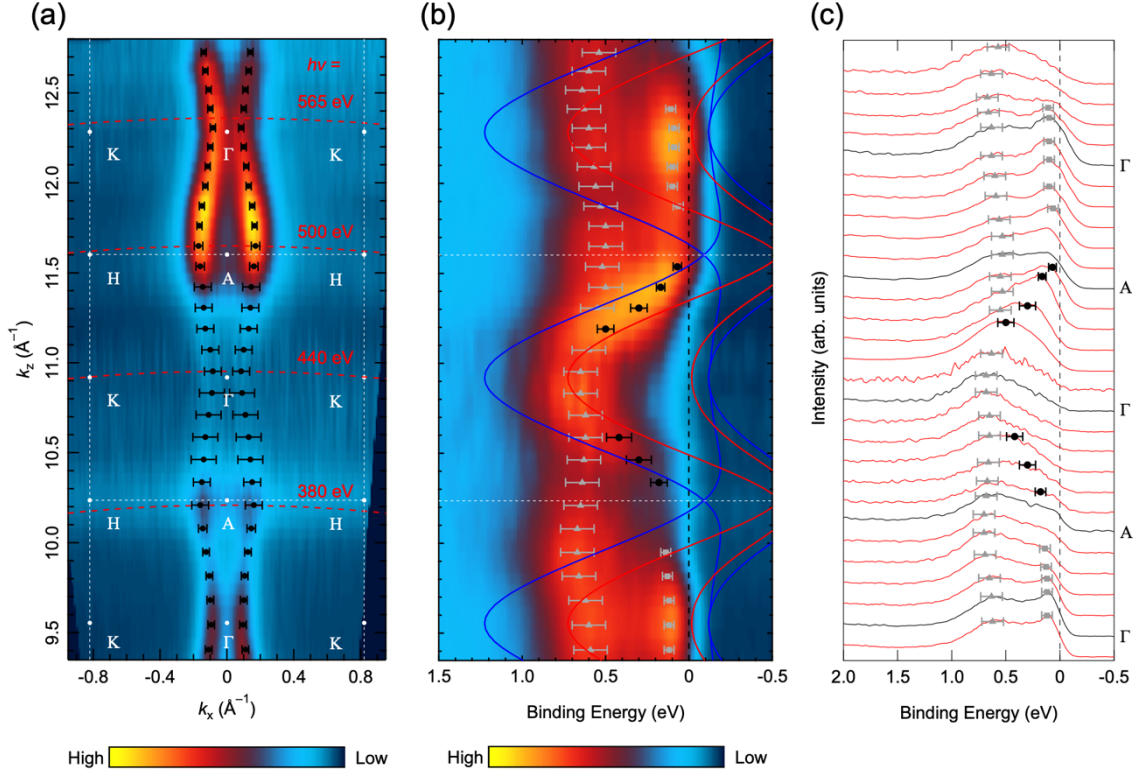


FIG. S12. (a) Out-of-plane FS map for the Ti_2O_3 films determined by photon-energy dependent ARPES images in the Γ -A-H-K emission plane. The FS map was obtained by plotting the ARPES intensity within the energy window of $E_F \pm 50$ meV. The data markers indicate the Fermi momentum (k_F) determined by fitting the momentum distribution curves (MDCs) of the corresponding ARPES image. The white dotted lines indicate the hexagonal BZ, and the red dotted arc lines represent the k paths passing through the A points (at photon energies of 500 eV and 380 eV) and the Γ points (at photon energies of 565 eV and 400 eV). (b) Experimental band structure along the Γ -A direction obtained by normal-emission ARPES. Black markers indicate the positions of the a_{1g} -derived band. Gray triangle and square markers indicate the positions of the surface-derived quasi-localized states and artifacts originating from the angle-integrated effects, respectively. For comparison purposes, the calculated band dispersions with $U = 0$ eV and 2.2 eV are overlaid as red and blue lines, respectively. (c) Corresponding normal-emission ARPES spectra along the Γ -A direction. The spectra were picked up from the photon-energy dependent ARPES images shown in Fig. S13.

3.3 ARPES images taken at different photon energies

The existence of the highly dispersive a_{1g} -derived band along the Γ –A direction is further confirmed by the photon-energy dependent ARPES images. Figure S13 shows representative ARPES images taken at different photon energies from 440 to 510 eV. In addition to the highly dispersive e_g^π -derived band, which forms the open hole FS along the BZ center line [Fig. S12(a)], another feature is observed in the ARPES images for $h\nu = 460$ – 490 eV. The additional band is attributed to the a_{1g} -derived band along the Γ –A direction in comparison with the DFT calculation (Fig. S4) [10]. The a_{1g} -derived band approaches E_F with increasing $h\nu$ and may cross E_F around the A point, forming a closed FS at the A point as predicted from the DFT calculation (see Fig. 4 and Figs. S8 and S9).

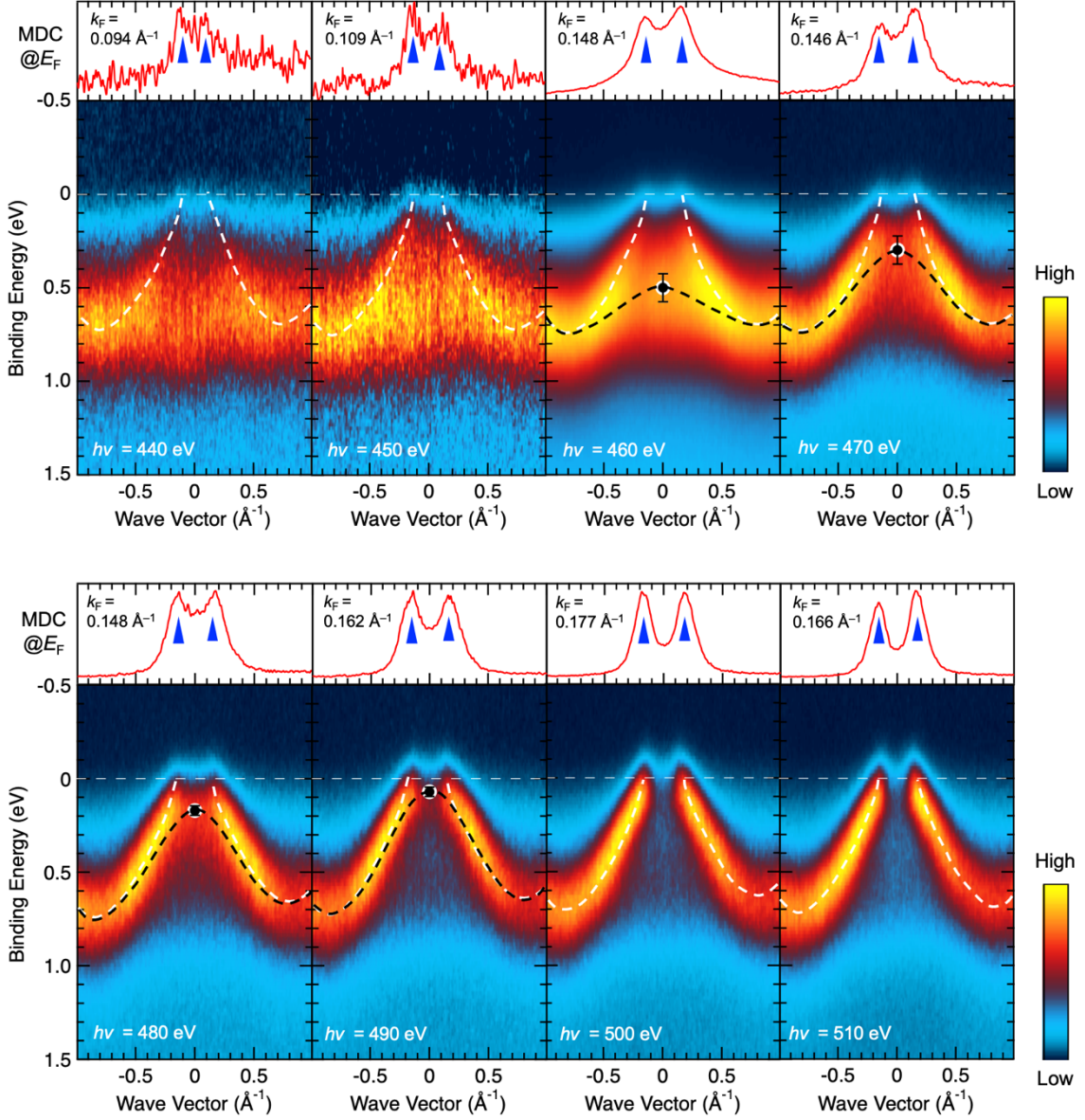


FIG. S13. Photon-energy dependence of ARPES images taken in the photon energy range of 440–510 eV. The white and black dotted lines are visual guides for the band dispersions of e_g^π -derived and a_{1g} -derived bands, respectively. The MDCs at E_F are also shown at the top panel of each ARPES image. The blue triangles indicate the position of k_F . The outer e_g^π -derived band forms a hole pocket at the zone center irrespective of $h\nu$ (k_z), whereas the top of the a_{1g} -derived band located below E_F at $h\nu = 460$ eV approaches E_F with increasing $h\nu$ and eventually crosses E_F (degenerate with the e_g^π -derived band) at $h\nu = 500$ eV (the A point). The data markers correspond to those in Figs. S12(b) and (c).

3.4 Fermi surface mapping for Ti_2O_3 films in the Γ -K-M and A-H-L planes

Figure S14 shows the FS maps taken at different photon energies for the A-H-L (taken at $h\nu = 500$ and 382 eV) and Γ -K-M (taken at $h\nu = 565$ and 440 eV) emission planes. Note that Figs. S14(a) and (b) are the same as the left and right sides of Fig. 2(d), respectively. The observed triangular-like FS around the A point in Fig. S14(a) is reversed at the other A point of one point below [Fig. S14(c)], reflecting the original trigonal symmetry of Ti_2O_3 . Together with the overall threefold intensity pattern of the observed FS, the results provide evidence that the present ARPES measurements observe the “bulk” electronic structures of Ti_2O_3 .

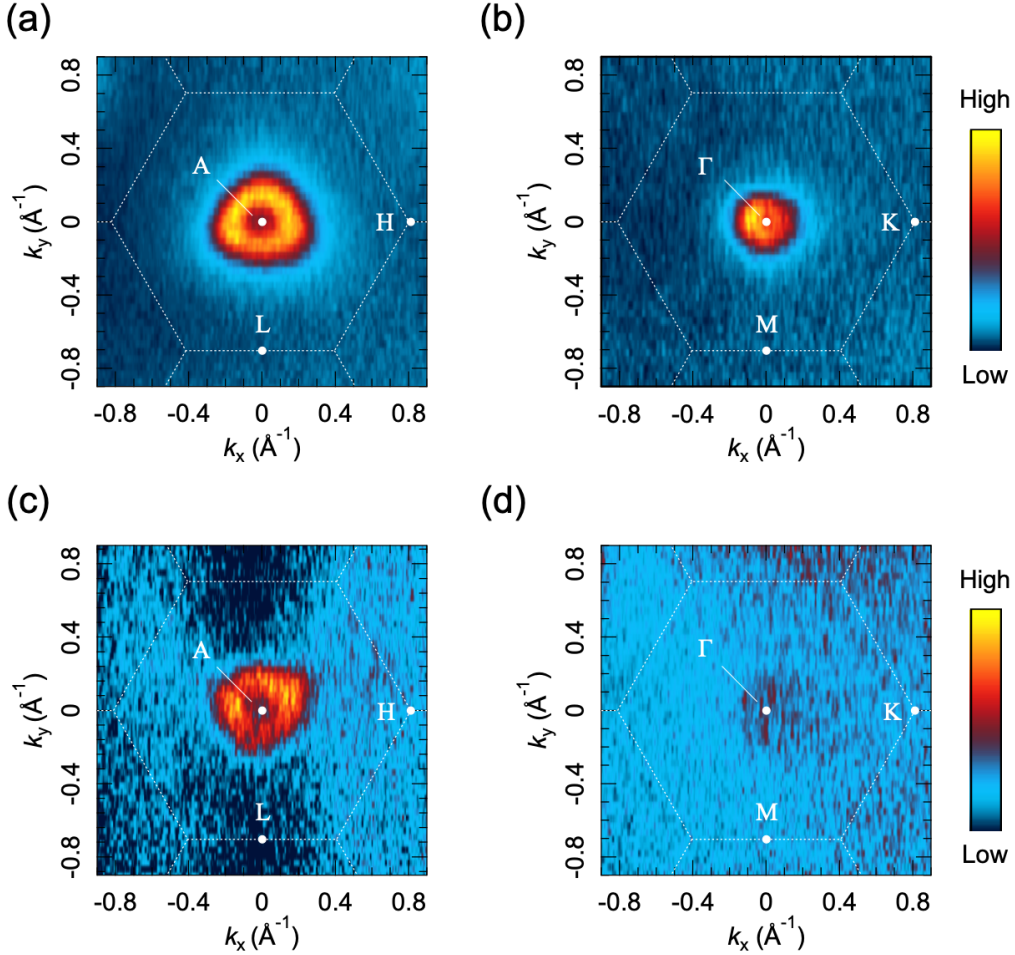


FIG. S14. FS maps of the Ti_2O_3 films acquired at constant photon energies of (a) 500 eV, (b) 565 eV, (c) 382 eV, and (d) 440 eV by changing emission angles. The hexagonal BZs are overlaid as the white dotted lines on the FS maps. The FS maps were obtained by plotting the ARPES intensity within the energy window of $E_F \pm 50$ meV. The much weaker intensity at the A and Γ points of one point below (382 eV and 440 eV) is due to the matrix-element effects (see Fig. S12).

3.5 Energy distribution curves along the A–H and Γ –K directions

Figures S15(a) and (b) show the energy distribution curves (EDCs) of the Ti_2O_3 films obtained at photon energies of 500 eV (corresponding to the A–H line) and 565 eV (corresponding to the Γ –K line), respectively. Dispersive features are clearly observable in the EDCs. Note that the seeming “peak” structure at the Γ point is due to the angle-integrated effect and close proximity of the hole FS with high intensity.

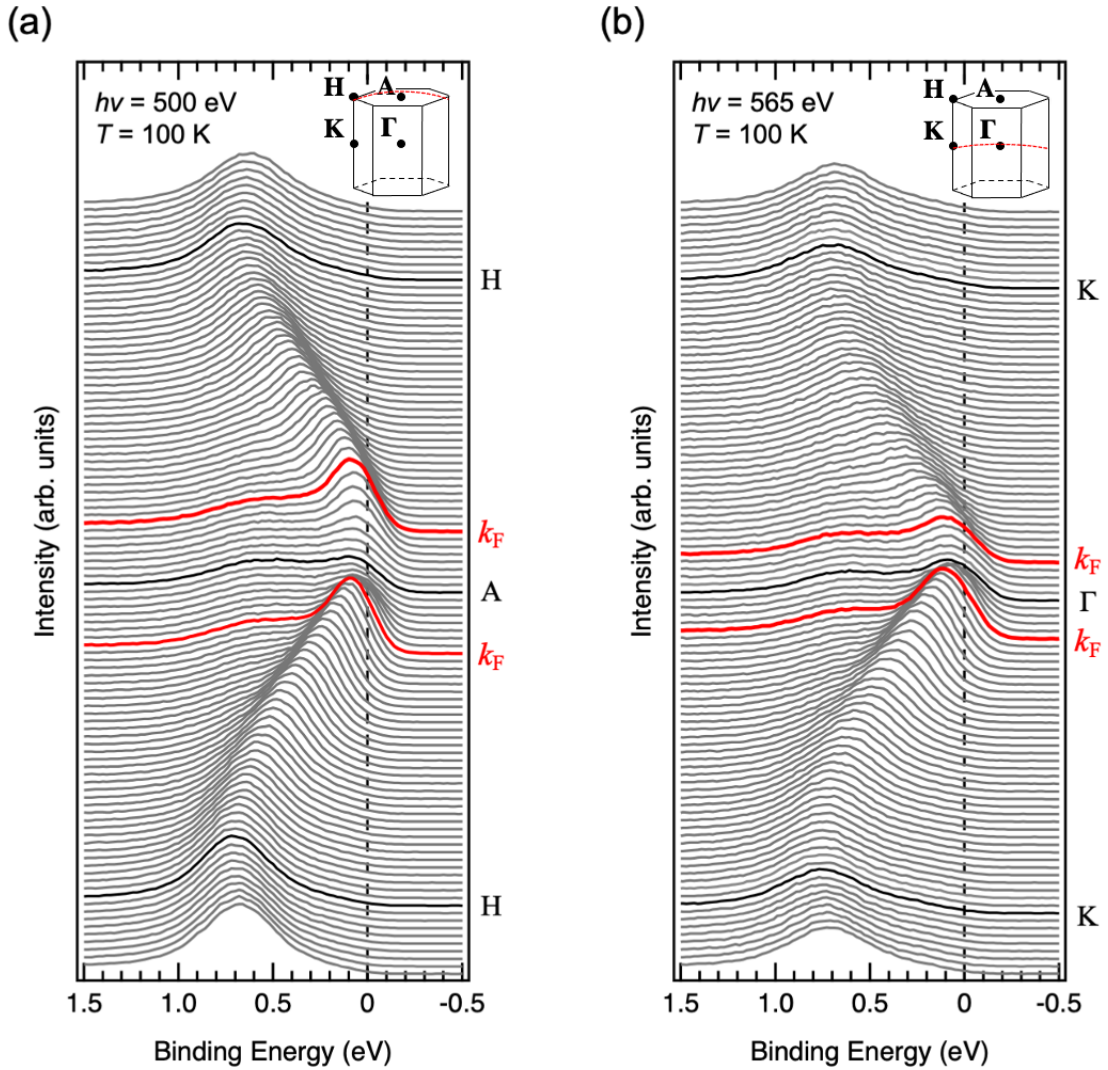


FIG. S15. EDCs (ARPES spectra) of the Ti_2O_3 films taken along the (a) A–H and (b) Γ –K directions. The corresponding measurement lines in the BZ are indicated by the red dotted arc lines in each inset.

Reference

[S1] M. Kawamura, “FermiSurfer: Fermi-surface viewer providing multiple representation schemes” *Comp. Phys. Commun.* **239**, 197–203 (2019). [DOI: 10.1016/j.cpc.2019.01.017](https://doi.org/10.1016/j.cpc.2019.01.017).